

---

**This manuscript has been submitted for publication in *Geochimica et Cosmochimica Acta*. This manuscript is under review and has yet to be accepted for publication. Subsequent versions of this manuscript may have slightly different content. If accepted, the final version of this manuscript will be available via the ‘Peer-reviewed Publication DOI’ link on the right-hand side of this webpage.**

---

**Paired  $\Delta_{47}$  and  $\Delta_{48}$  analyses and model calculations constrain equilibrium, experimentally-manipulated kinetic isotope effects, and mixing effects in calcite**

Jamie Lucarelli<sup>1</sup>, Bettina Purgstaller<sup>2</sup>, Zeeshan Parvez<sup>1</sup>, James M. Watkins<sup>3</sup>, Robert A. Eagle<sup>1</sup>, Martin Dietzel<sup>2</sup>, Aradhna Tripathi<sup>1</sup>

<sup>1</sup>Department of Earth, Planetary, and Space Sciences, Department of Atmospheric and Oceanic Sciences, Institute of the Environment and Sustainability, Center for Diverse Leadership in Science, UCLA, Los Angeles, CA 90095 USA.

<sup>2</sup>Institute of Applied Geosciences, Graz University of Technology, 8010 Graz, Austria

<sup>3</sup>Department of Earth Science, University of Oregon, Eugene, OR 97403 USA  
Correspondence to: [jklucarelli@gmail.com](mailto:jklucarelli@gmail.com) and [atripathi@g.ucla.edu](mailto:atripathi@g.ucla.edu)

1 **Paired  $\Delta_{47}$  and  $\Delta_{48}$  analyses and model calculations constrain equilibrium, experimentally-**  
2 **manipulated kinetic isotope effects, and mixing effects in calcite**

3

4 *Geochimica et Cosmochimica Acta*

5

6 Jamie Lucarelli<sup>1</sup>, Bettina Purgstaller<sup>2</sup>, Zeeshan Parvez<sup>1</sup>, James M. Watkins<sup>3</sup>, Robert A. Eagle<sup>1</sup>, Martin  
7 Dietzel<sup>2</sup>, Aradhna Tripathi<sup>1</sup>

8

9 <sup>1</sup>Department of Earth, Planetary, and Space Sciences, Department of Atmospheric and Oceanic Sciences,  
10 Institute of the Environment and Sustainability, Center for Diverse Leadership in Science, UCLA, Los  
11 Angeles, CA 90095 USA.

12 <sup>2</sup>Institute of Applied Geosciences, Graz University of Technology, 8010 Graz, Austria

13 <sup>3</sup>Department of Earth Science, University of Oregon, Eugene, OR 97403 USA

14 Correspondence to: jklucarelli@gmail.com and atripati@g.ucla.edu

15

16 **Abstract**

17

18 The high-precision analysis of the abundance of the dominant  $m/z$  47 CO<sub>2</sub> isotopologue derived  
19 from acid digestion of carbonate minerals (<sup>13</sup>C<sup>18</sup>O<sup>16</sup>O; denoted by  $\Delta_{47}$ ) forms the basis for carbonate  
20 clumped isotope thermometry. Since the first measurements were published 16 years ago, considerable  
21 effort has gone into characterizing the relationship between  $\Delta_{47}$  and carbonate precipitation temperature,  
22 and in identifying carbonates that do not achieve isotopic equilibrium. Mass spectrometry is now capable  
23 of the paired measurement of the primary  $m/z$  47 and  $m/z$  48-isotopologues ( $\Delta_{47}$  and  $\Delta_{48}$ ; <sup>12</sup>C<sup>18</sup>O<sub>2</sub> is  
24 denoted by  $\Delta_{48}$ ), which has the potential to place additional constraints on kinetic isotope effects in  
25 carbonate minerals and trace distinct reaction pathways. Here, we explored factors that contribute to  
26 calcite mineral equilibrium and disequilibrium in  $\Delta_{47}$  and  $\Delta_{48}$  using a combination of experiments and  
27 theoretical calculations with three types of models. We precipitated calcite at pH 8.3 with carbonic  
28 anhydrase (CA) to approach quasi-isotopic equilibrium in the dissolved inorganic carbon pool and report  
29 values for  $\Delta_{47}$ ,  $\Delta_{48}$ , and oxygen isotopes ( $\delta^{18}\text{O}$ ) for calcite grown over a temperature range from 5 to 25 °C  
30 and compare our findings to predictions from an ion-by-ion model that support equilibrium precipitation.  
31 We also compare results to the Devils Hole slow-growing cave calcite, and other published temperature  
32 calibration data. We report the following combined equilibrium calibration relationships:  $\Delta_{48}^{\text{CDES } 90} =$   
33  $(0.429 \pm 0.010) \Delta_{47}^{\text{CDES } 90} - (0.006 \pm 0.006)$ ;  $r^2 = 0.98$ ;  $\Delta_{47}^{\text{I-CDES}} = (0.037 \pm 0.001) \times 10^6 T^{-2} + (0.178 \pm$   
34  $0.009)$ ;  $r^2 = 0.99$ ;  $\Delta_{48}^{\text{CDES } 90} = (0.015 \pm 0.0005) \times 10^6 T^{-2} + (0.078 \pm 0.006)$ ;  $r^2 = 0.98$ . We used paired  
35 measurements of  $\Delta_{47}$  and  $\Delta_{48}$  to constrain kinetic isotope effects in calcite precipitated at pH ranging from  
36 8.3-11 and temperatures from 5 to 25 °C, with and without CA present, and observe kinetic enrichments  
37 in  $\Delta_{47}$ , negative (hyperstochastic) values for  $\Delta_{48}$ , and depleted values of  $\delta^{18}\text{O}$ , compared to equilibrium  
38 values. Experimentally constrained kinetic trajectories, when compared with an ion-by-ion model and

39 IsoDIC theoretical predictions, are consistent with CO<sub>2</sub> hydration/hydroxylation. Mixing drives elevated  
40  $\Delta_{47}$  and  $\Delta_{48}$  values and was assessed using mixing experiments with endmembers of varying isotopic  
41 compositions and compared to a  $\Delta_{47}$  and  $\Delta_{48}$  mixing model that constrains nonlinear mixing trajectories  
42 for calcite. While mixing may induce artifacts in two-component mixtures when endmember bulk  
43 compositions differ by more than 7 ‰, or if endmember  $\Delta_{47}$  and  $\Delta_{48}$  differ by more than 0.03 ‰, this  
44 should be detectable and potentially correctible using paired clumped isotope measurements and is  
45 unlikely to be important for some materials.

## 46 47 48 **1. Introduction** 49 50

51 Carbonate clumped isotope thermometry is based on the frequency with which rare, heavy  
52 isotopes of carbon (<sup>13</sup>C) or oxygen (<sup>18</sup>O) in carbonate minerals are bonded to each other relative to a  
53 stochastic (random) distribution (Wang et al., 2004; Eiler and Schauble, 2004; Ghosh et al., 2006;  
54 Schauble et al., 2006). The dominant clumped isotopologue measured in carbonate minerals from  
55 phosphoric acid digestion of carbonates is <sup>13</sup>C<sup>18</sup>O<sup>16</sup>O and has a mass of 47 amu ( $\Delta_{47}$ ), while <sup>12</sup>C<sup>18</sup>O<sup>18</sup>O is  
56 the dominant mass-48 isotopologue ( $\Delta_{48}$ ). The use of  $\Delta_{47}$  and  $\Delta_{48}$  as paleothermometers rely on  
57 equilibrium clumped isotope fractionation in the carbonate mineral lattice. However, recent theoretical  
58 and experimental work has shown that some biogenic and abiogenic carbonates yield disequilibrium  $\Delta_{47}$   
59 (Ghosh et al., 2006; Daëron et al., 2011, Saenger et al., 2012, Tang et al., 2014; Tripathi et al., 2015; Guo et  
60 al., 2019; Daëron et al., 2019) and  $\Delta_{48}$  values (Tripathi et al., 2015; Guo, 2020; Bajnai et al., 2020;  
61 Lucarelli et al., 2021; Fiebig et al., 2021).

62 The paired measurement of  $\Delta_{47}$  and  $\Delta_{48}$  has been theoretically (Hill et al., 2014; Tripathi et al.,  
63 2015; Guo, 2020; Hill et al., 2020) and experimentally (Fiebig et al., 2019; Bajnai et al., 2020; Swart et  
64 al., 2021; Lucarelli et al., 2021; Fiebig et al., 2021) shown to have a characteristic equilibrium  
65 relationship. The equilibrium  $\Delta_{47}$ - $\Delta_{48}$  relationship along with constrained boundaries of disequilibrium  
66 trajectories in dissolved inorganic carbon (DIC) pools and in carbonate minerals may be used to identify  
67 the origin of kinetic isotope effects (Tripathi et al., 2015; Bajnai et al., 2020; Guo, 2020) and used to  
68 correct for such effects and derive expected equilibrium clumped isotope values from samples (Bajnai et  
69 al., 2020; Guo, 2020).

70 Through comparison of theoretical predictions with experimental data, a robust framework can be  
71 developed to advance the paired carbonate clumped isotope approach as a potential tool for constraining  
72 kinetic isotope effects (KIEs), including vital effects in biogenic carbonates. Currently, the paired  $\Delta_{47}$  and  
73  $\Delta_{48}$  trajectory of kinetic isotope effects (KIEs) in carbonates is limited to theory with calculations for a  
74 DIC pool at equilibrium (Hill et al., 2014; Tripathi et al., 2015), hydration/hydroxylation (Guo, 2020), and  
75 for growth from a solution of DIC with cations present (Hill et al., 2020). Theory has been used to explain  
76 some measurements of disequilibrium  $\Delta_{47}$  values in corals, speleothems, and high pH travertines (Guo,  
77 2020), and disequilibrium  $\Delta_{47}$  and  $\Delta_{48}$  values in speleothems, stalagmites, and corals (Bajnai et al., 2020).

78 Here, we adapted experimental approaches used in Tang et al. (2014) and Tripathi et al. (2015) to  
79 constrain KIEs in  $\Delta_{47}$ ,  $\Delta_{48}$ , and  $\delta^{18}\text{O}$  in calcite precipitated under controlled conditions at different pH and  
80 temperatures, with and without the addition of the enzyme carbonic anhydrase (CA). We compared data  
81 from calcite grown under isotopic disequilibrium conditions at varying pH to calcite formed at quasi-  
82 equilibrium conditions. We measured samples to further constrain equilibrium and kinetically governed

83 relationships for clumped isotopes, including  $\Delta_{47}$ - $\Delta_{48}$ ,  $\Delta_{47}$  and  $T$ ,  $\Delta_{48}$  and  $T$ , and bulk  $\delta^{18}\text{O}$  and  $\delta^{13}\text{C}$  and  
 84 clumped isotopes, and compared experimental results to model calculations. We constructed and used a  
 85 numerical mixing model and predicted nonlinear effects in  $\Delta_{47}$  and  $\Delta_{48}$  and compared results to  
 86 experimental data.

87

## 88 2. Background

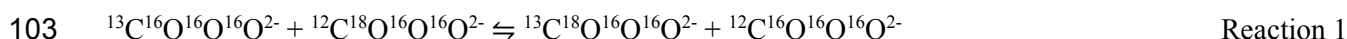
89

### 90 2.1 Carbonate clumped isotopes and notation

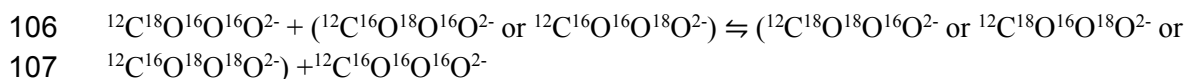
91

92 Historically, carbonate clumped isotope thermometry used the deviations in the abundance of the  
 93  $m/z$  47  $\text{CO}_2$  isotopologue,  $^{16}\text{O}-^{13}\text{C}-^{18}\text{O}$ , which is liberated from the phosphoric acid digestion of the most  
 94 abundant (67 ppm)  $m/z$  63 carbonate isotopologue,  $^{13}\text{C}-^{16}\text{O}-^{16}\text{O}-^{18}\text{O}$ , relative to a stochastic distribution of  
 95 isotopologues (Ghosh et al., 2006). Recent developments in mass spectrometry precision, such as the use  
 96 of secondary electron suppression and  $10^{13} \Omega$  resistors, has enabled the accurate measurement of the  
 97 lower abundance  $m/z$  48  $\text{CO}_2$  isotopologue,  $^{18}\text{O}-^{12}\text{C}-^{18}\text{O}$ , which is liberated from the phosphoric acid  
 98 digestion of the most abundant (12 ppm)  $m/z$  64 carbonate isotopologue,  $^{12}\text{C}-^{16}\text{O}-^{18}\text{O}-^{18}\text{O}$  (Ghosh et al.,  
 99 2006). The thermodynamic equilibrium relationship between  $m/z$  63 and  $m/z$  64 isotopologues with  
 100 precipitation temperature is governed by the equilibrium constant,  $K$ , in Reactions 1 and 2 (Wang et al.,  
 101 2004; Ghosh et al., 2006).

102



104



108

109 When  $m/z$  63 and 64 carbonate isotopologues are digested in phosphoric acid, one oxygen is cleaved, and  
 110 the resulting excess  $m/z$  47 and 48  $\text{CO}_2$ , respectively, is measured on an isotope ratio mass spectrometer  
 111 and described as

$$112 \quad \Delta_{47} = (R_{47\text{sample}}/R_{47\text{stochastic}} - 1) \quad (1)$$

113

$$114 \quad \Delta_{48} = (R_{48\text{sample}}/R_{48\text{stochastic}} - 1) \quad (2)$$

115

116 where  $R_i$  is the ratio of  $i/44$   $\text{CO}_2$  isotopologues, and  $\Delta_{47}$  and  $\Delta_{48}$  are given in parts per thousand (‰)  
 117 (Ghosh et al., 2006; Eiler et al., 2007).

118

### 119 2.2 Disequilibrium processes in carbonates

120

121  $\Delta_{47}$  data for some abiotic and biogenic carbonates have been shown to record precipitation out of  
 122 isotopic equilibrium (Affek et al., 2008; Daeron et al., 2011; Saenger et al., 2012; Tang et al., 2014;

123 Tripathi et al., 2015; Kimball et al., 2016; Daëron et al., 2019; Bajnai et al., 2020). This can be correlated  
124 with  $\delta^{18}\text{O}$  disequilibria and observed in experiments at elevated pH (e.g., Tang et al., 2014). Multiple  
125 coral species are known to significantly elevate the pH of their calcifying fluid (Ghosh et al., 2006; Affek  
126 et al., 2008; Trotter et al., 2011; Anagnostou et al., 2012; Adkins et al., 2003; Saenger et al., 2012;  
127 Kimball et al., 2016; Spooner et al., 2016). Strongly alkaline abiotic carbonate precipitation occurs in  
128 surface and subsurface aqueous systems, such as alkaline springs with pH > 11 (Christensen et al., 2021).

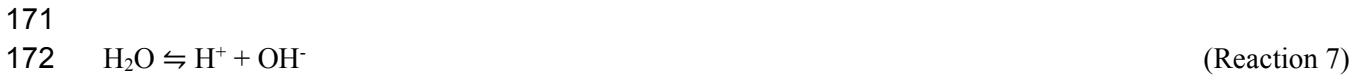
129 Multiple mechanisms have been proposed to explain  $\Delta_{47}$  isotope disequilibrium mineral  
130 compositions. They have been observed experimentally at elevated pH (Tang et al., 2014). Clumped  
131 isotopic disequilibrium can arise from mineral growth from a DIC pool that is at equilibrium with DIC  
132 from speciation effects (e.g., Hill et al., 2014; Tripathi et al., 2015; Watkins and Hunt, 2015; Hill et al.,  
133 2020). Carbonate mineral precipitation can occur before isotopic equilibration of dissolved inorganic  
134 carbon (DIC) (Beck et al. 2005; Tripathi et al., 2015; Staudigal and Swart, 2018).  $\text{CO}_2$  hydration and  
135 hydroxylation reactions are another potential source of isotopic disequilibrium (Staudigal and Swart,  
136 2018; Guo, 2020; Boettger and Kubicki, 2021), as are dehydration and dehydroxylation reactions, and  
137 these can arise from  $\text{CO}_2$  absorption and degassing processes (Daëron et al., 2011; Guo, 2020). Aqueous  
138 ion and  $\text{CO}_2$  gas diffusion (Thiagarajan et al., 2011), and organism-specific vital effects from enzymatic  
139 activity and metabolism have also been hypothesized to give rise to clumped isotope disequilibrium.  
140 Clumped isotopic disequilibrium in the DIC pool has been hypothesized to be modulated by carbonate  
141 precipitation rate (Tripathi et al., 2015), as with other geochemical systems such as oxygen isotopes  
142 (Dietzel et al., 2009; Watkins et al., 2014).

143 When carbonate minerals precipitate under isotopic disequilibrium conditions, KIEs originating  
144 from differing reaction rates of heavy versus light isotopologues can result in clumped isotope values that  
145 are higher or lower than equilibrium mineral clumped isotope values, which in turn can yield an over- or  
146 underestimation of precipitation temperature. Depending on carbonate mineral growth conditions, there  
147 are different trajectories for possible KIEs, and these can potentially be used to identify the process(es)  
148 involved through measurement of paired  $\Delta_{47}$  and  $\Delta_{48}$ , and bulk isotope values. However, these trajectories  
149 are not yet well constrained and are limited to only a few studies. DIC speciation effects that could get  
150 recorded in a growing mineral were explored in Tripathi et al. (2015). Recent modeling predictions from  
151 Guo (2020) has aimed to constrain KIEs in the  $\Delta_{47}$ ,  $\Delta_{48}$  and  $\delta^{18}\text{O}$  of the  $\text{HCO}_3^-$  endmember in hydration  
152 and hydroxylation reactions occurring during  $\text{CO}_2$  absorption, degassing, and DIC- $\text{H}_2\text{O}$  exchange. Bajnai  
153 et al. (2020) and Fiebig et al. (2021) constructed  $\Delta_{47}$  and  $\Delta_{48}$  slopes relative to an equilibrium regression to  
154 remove kinetic biases from warm and cold-water coral, brachiopod, belemnite, stalagmite, and  
155 speleothem samples.

### 156 157 **2.2.1 $\text{CO}_2$ hydration and hydroxylation**

159  $\text{CO}_2$  hydration (Reaction 3) and hydroxylation (Reaction 4) reactions are responsible for  $^{18}\text{O}/^{16}\text{O}$   
160 equilibration, as they are the only direct route for the exchange of O atoms between  $\text{H}_2\text{O}$  and DIC (Zeebe  
161 and Wolf-Gladrow, 2001). Clumped and oxygen isotope equilibration of DIC in an aqueous solution are  
162 also controlled by three additional key reactions (Reactions 5-7) (Guo, 2020).





173  
174 Equilibrium isotopic compositions are obtained when DIC and H<sub>2</sub>O have had sufficient time to  
175 isotopically equilibrate. When DIC and H<sub>2</sub>O have not been equilibrated, KIEs and disequilibrium isotopic  
176 compositions can arise. The parameters governing the time to reach isotopic equilibrium are the forward  
177 and reverse CO<sub>2</sub> hydration and hydroxylation kinetic rate constants, which depend on temperature (Zeebe  
178 and Wolf-Gladrow, 2001), and DIC speciation, which is function of temperature and pH (Uchikawa and  
179 Zeebe, 2012; Tripathi et al., 2015). The rate constant for hydration is not sensitive to ionic strength  
180 (Johnson, 1982; Miller et al., 1971; Knocke 1980; Zeebe and Wolf-Gladrow, 2001), whereas a subtle  
181 dependency has been documented for the hydroxylation rate constant (Johnson, 1982). Higher  
182 temperature results in faster reaction kinetics and thus faster isotopic equilibration of the DIC pool. A  
183 higher pH causes much longer isotopic equilibration times induced by extreme low molar fraction of  
184 aqueous CO<sub>2</sub> in DIC, leading CO<sub>2</sub> to be mostly unavailable for isotope exchange in Reactions 3 and 4  
185 (Beck et al., 2005; Weise and Kluge, 2020). For example, at 25 °C at pH of 8.7, <sup>18</sup>O equilibration is  
186 reached at ~17 hours, whereas at pH 12, <sup>18</sup>O equilibration is reached at ~35 days (Beck et al., 2005). At  
187 40 °C and a pH of 12, <sup>18</sup>O equilibration time is reduced to ~10 days (Beck et al., 2005).

### 188 189 **2.2.2 Carbonic anhydrase**

190  
191 The addition of the enzyme carbonic anhydrase (CA) catalyzes the forward and reverse hydration  
192 reaction and thus significantly decreases the time to reach isotopic equilibrium. The uncatalyzed  
193 hydration reaction rate at 25 °C and pH 7.4 is ~10<sup>-1</sup> s<sup>-1</sup>, while the CA catalyzed rate can reach ~10<sup>6</sup> s<sup>-1</sup>  
194 depending on [CA] (Kernohan, 1964), where highest catalyzation effects are achieved at pH > 8 (Berg et  
195 al., 2002). Many marine calcifiers used for climate reconstructions are thought to have CA within their  
196 calcifying space, including coccolithophores (Nimer et al., 1994; Soto et al., 2006) and other  
197 phytoplankton (Rost et al., 2003), oysters (Miyamoto et al., 1996; Yu et al., 2006), scleractinian coral (Al-  
198 Horani et al., 2003; Moya et al., 2008; Bertucci et al, 2011), and benthic foraminifera (de Goeyse et al.,  
199 2019). The role that CA plays in calcification is not completely known, including the effectiveness of CA  
200 at reducing clumped and bulk KIEs at high pH and varying temperatures.

### 201 202 **2.2.3 Mixing effects**

203  
204 Numerical models and experimentation have shown that while  $\delta^{13}\text{C}$ ,  $\delta^{18}\text{O}$ ,  $\delta^{45}$ ,  $\delta^{46}$ , and  $\delta^{47}$  mix  
205 linearly,  $\Delta_{47}$  mixes non-linearly (Eiler and Schauble, 2004; Defliese and Lohmann, 2015). Thus, in  
206 addition to KIEs, mixing effects from the homogenization of isotopically heterogeneous samples can  
207 result in measured  $\Delta_{47}$  values that do not accurately reflect precipitation temperature (Defliese and  
208 Lohmann, 2015). Some samples that are commonly used for  $\Delta_{47}$ -based temperature reconstructions  
209 display isotopic heterogeneity in isotopically distinct growth bands or multiple cementation stages (Jones

210 et al., 2015), and thus sampling that integrates over growth increments or cements has the potential to  
211 give rise to mixing effects.

212  
213

### 214 3. Methods

215  
216

#### 217 3.1 Calcite precipitation experiments

218

219 Calcite was precipitated under controlled conditions at pH 8.3, 9.0, 9.5, 10.0, 10.5, and 11.0 at 5  
220 °C, 10 °C, 15 °C, and 25 °C, with and without the addition of CA (molecular weight 29,000 g/mol). CA  
221 has been shown to be active in catalyzing CO<sub>2</sub> hydration at all pH values used in our experiment  
222 (Kernohan, 1964). Experimental conditions are given in Table 1. Calcite was precipitated by using a  
223 method adapted from Dietzel et al. (2004). A schematic of the precipitation apparatus is shown in Figure  
224 1. In all experiments, a 0.5 L bottle that is 2 mm thick polyethylene is filled with 0.83 M NaHCO<sub>3</sub> and 2  
225 M HCl and placed inside a 5 L outer container filled with 4.9 L Milli Q water, 10 mM CaCl<sub>2</sub>, 0.01 mM  
226 SrCl<sub>2</sub>, 50 mM NaCl, and no DIC. All chemicals are reagent grade from Merck.

227 The pCO<sub>2</sub> gradient between the inner and outer containers causes CO<sub>2</sub> gas to diffuse through the  
228 polyethylene membrane into the outer container solution where the CO<sub>2</sub> reacts to form carbonate ions that  
229 precipitate as CaCO<sub>3</sub>. The outer solution was constantly stirred with a large floating stir bar by placing the  
230 containers on top of a stir plate at 200 rpm. A piece of Styrofoam was placed in between the stir plate and  
231 solution to prevent temperature changes. The pH of the outer container solution was held constant by a  
232 Schott TitroLine alpha plus titrator (± 0.03 accuracy) with 2 M NaOH. The entire precipitation apparatus  
233 was placed inside an Aqualytic Thermostatic Cabinet (± 0.5 °C accuracy) to hold the precipitation  
234 temperature constant. In experiments with CA, 0.25 μM CA is added to the outer solution. A  
235 concentration of 0.25 μM CA should be sufficient to maintain oxygen isotopic equilibrium among DIC  
236 species up to at least pH = 9.3 (Watkins et al., 2014). Each experiment yielded 30-40 mg of precipitate.  
237 The mineralogy of the precipitate was determined by X-ray powder diffraction (XRD) PANalytical  
238 X'Pert PRO diffractometer. The mineral phase was determined using PANalytical X'Pert HighScore  
239 Plus software.

240 Every 2-3 days a 2 ml sample of the solution was removed from the outer solution via a syringe  
241 that was inserted into an airtight port through the lid of the apparatus. The solution was filtered through a  
242 0.2 μm cellulose acetate membrane to remove any precipitate and subsequently analyzed for trace  
243 elements on a Perkin Elmer Optime 4300DV Inductively Coupled Plasma - Optical Emission  
244 Spectrometer (ICP-OES). This analysis yielded the [Ca], allowing for the estimation of the precipitation  
245 rate by  $([Ca]_{\text{final}} - [Ca]_{\text{initial}}) / (t_{\text{final}} - t_{\text{initial}})$ , which was converted to mol s<sup>-1</sup> m<sup>-2</sup> using the specific surface  
246 area of 0.27 m<sup>2</sup>/g (Tang et al., 2008). Oxygen isotopes of the precipitation solution were measured at the  
247 start and end of most experiments by wavelength-scanned cavity ring-down spectroscopy (WS-CRDS)  
248 using a Picarro L2140-i system. Typical analytical precision (1 σ) was ±0.05 ‰ for δ<sup>18</sup>O<sub>water</sub>, where the  
249 values are referenced relative to the Vienna Standard Mean Ocean Water (VSMOW).

250

#### 251 3.2 Mixing experiments

252

253 Two internal carbonate standards, CM Tile and Mallinckrodt, were used as isotopic endmembers  
254 to constrain  $\Delta_{48}$  mixing effects. These standards were selected as endmembers because they have greatly  
255 varying bulk and clumped isotope values (see Table 5), with a  $\sim 20$  ‰ difference in  $\delta^{18}\text{O}$ ,  $\sim 38$  ‰  
256 difference in  $\delta^{13}\text{C}$ , 0.164 ‰ difference in  $\Delta_{47}$ , and 0.062 ‰ difference in  $\Delta_{48}$ . Endmembers with large  
257 differences in isotopic values have been shown to have a greater magnitude of mixing effects than  
258 endmembers with smaller isotopic differences (Defliese et al., 2015).

259 The two endmembers were combined into three mixes with varying contributions from each  
260 endmember. Mix 1 was 75 % Mallinckrodt and 25 % CM Tile, Mix 2 was 50 % Mallinckrodt and 50 %  
261 CM Tile, and Mix 3 was 25 % Mallinckrodt and 75 % CM Tile. The mixes were created by weighing out  
262 the carbonate powder from each sample and pouring them into a glass vial, where they were first stirred  
263 with a spatula, then shaken by hand for several minutes. The mixtures were then crushed in a mortar and  
264 pestle to equalize grain size, then remixed with a spatula and shaken in a glass vial. Each endmember and  
265 mix were analyzed for  $\Delta_{47}$ ,  $\Delta_{48}$ ,  $\delta^{13}\text{C}$ ,  $\delta^{18}\text{O}$ . The observed change in  $\Delta_{47}$  and  $\Delta_{48}$  values due to mixing  
266 effects is referred to as  $T$ , described in Equation 3:

$$267$$
$$268 T_i = \Delta_{i \text{ endmember}} - \Delta_{i \text{ mix}} \quad (3)$$
$$269$$

270 where  $\Delta_{i \text{ endmember}}$  is the  $\Delta_{47}$  or  $\Delta_{48}$  of the endmember with the highest value. It represents clumped isotope  
271 enrichment beyond what would be observed in linear mixing.

272

### 273 3.3 Clumped isotope instrumentation

274

275 Standards and samples were analyzed on three isotope ratio mass spectrometers (IRMS) during  
276 2018-2021. The instruments used in this work were a Thermo Fisher MAT 253, and two Nu Instruments  
277 Perspective mass spectrometers, with both Nu Instruments having multiple configurations (Table 2). All  
278 instrumental configurations used here have been shown to produce statistically indistinguishable  $\Delta_{47}$   
279 (Upadhyay et al., 2021; Lucarelli et al., 2021) and the Nu Instruments produce statistically  
280 indistinguishable  $\Delta_{48}$  data (Lucarelli et al., 2021). Only data from the Nu Instruments are used in the  $\Delta_{48}$   
281 analyses reported here.

282 A typical daily run on all instruments consists of five samples and five standards, with standards  
283 bracketing the samples. Raw data was processed and corrected in Easotope 64-bit version from release  
284 20201231 (John and Bowen, 2016) using the IUPAC parameter set (Brand et al., 2010; Daëron et al.,  
285 2016).  $\Delta_{47}$  data are presented relative to international standards ETH-1, ETH-2, ETH-3 in the I-CDES  
286 reference frame (Bernasconi et al., 2021) at 90 °C,  $\Delta_{47 \text{ I-CDES}}$ .  $\Delta_{48}$  data are presented relative to the same  
287 carbonate standards, with the addition of the in-house carbonate standard, Veinstrom (Upadhyay et al.,  
288 2021; Lucarelli et al., 2021), in the 90 °C reference frame,  $\Delta_{48 \text{ CDES } 90}$ .

289 The Thermo Fisher MAT 253 used an autosampler similar to what is described in Passey and  
290 Henkes (2010) with a 105 weight % phosphoric acid bath held at 90 °C. After carbonate samples of 4-7  
291 mg are digested,  $\text{CO}_2$  (g) is cryogenically purified through traps containing dry ice-cooled ethanol and  
292 liquid nitrogen, which remove low vapor pressure gases such as  $\text{H}_2\text{O}$  (g). The  $\text{CO}_2$  passed through  
293 elemental silver wool (Sigma Aldrich), followed by a -20 °C gas chromatograph (GC) that contains  
294 Porapak Type-Q™ 50/80 mesh column pack material with He carrier gas. The  $m/z$  44 beam intensity is  
295 16000 mV. There are a total of 80-90 cycles of sample-standard comparison with a total integration time  
296 of 720 s.

297 Nu Instruments Perspective configurations 1a, 1b, and 1c (Table 2) consist of the same mass  
 298 spectrometer with differences in the reaction and digestion system. Thus, the sample purification method,  
 299 acid digestion temperature, and acid digestion method differ. All configurations on this instrument used a  
 300 sample size of 0.4-0.6 mg with a total of 60 cycles of sample-standard comparison with a total integration  
 301 time of 1200 s. This instrument is equipped with two curved plates with a voltage difference in front of  
 302 the Faraday collectors for  $m/z$  47-49 to perform secondary electron suppression, which makes the linearity  
 303 correction an order of magnitude smaller than on the Thermo Fisher MAT 253. Nu Instruments  
 304 Perspective configuration 1a used the same autosampler setup as the MAT 253 with an acid digestion  
 305 temperature of 90 °C, common acid bath, GC, He carrier gas, and cryogenic purification traps. New  
 306 Instruments Perspective 1b is identical to 1a, except for the sample purification method, which used a  
 307 relatively short GC column called an adsorption trap that is under vacuum (no carrier gas) and contains  
 308 Poropak Type Q<sup>TM</sup>. New Instruments Perceptive 1c used an acid digestion temperature of 70 °C with  
 309 individual glass reaction vials and an adsorption trap. Nu Instruments Perspective 2a and 2b use the same  
 310 mass spectrometer with differences in the acid digestion temperature and method. Nu Instruments  
 311 Perspective 2a used a 90 °C acid digestion temperature, common acid bath, and adsorption trap. Nu  
 312 Instruments Perspective Config. 1b used 70 °C acid digestion, individual glass sample vials, and an  
 313 adsorption trap. Both configurations used samples from 0.4-0.6 mg, and had 60 cycles of sample-standard  
 314 comparison with a total integration time of 1200 s.

315

### 316 3.4 Converting $\Delta_{47}$ and $\Delta_{48}$ to $\Delta_{63}$ and $\Delta_{64}$

317

318 Measured  $\Delta_{47}$  and  $\Delta_{48}$  were converted to theoretical calcite mineral  $\Delta_{63}$  and  $\Delta_{64}$ , respectively, for  
 319 direct comparison to model predictions for kinetic and equilibrium relationships between bulk and  
 320 clumped isotopes. This conversion was carried out using equations from Lucarelli et al. (2021). In  
 321 summary, regressions were determined for compositionally dependent acid digestion fractionation factors  
 322 (AFFs),  $\Delta_{63-47}^*$  and  $\Delta_{64-48}^*$ , by using model predicted  $\Delta_{63}$  and  $\Delta_{64}$  values for calcite precipitated at 600 °C  
 323 and 33.7 °C (Hill et al., 2014; Tripathi et al., 2015). The difference was calculated between the model-  
 324 predicted  $\Delta_{63}$  and  $\Delta_{64}$  and experimentally determined  $\Delta_{47}$  and  $\Delta_{48}$  for ETH-1 and ETH-2, calcite standards  
 325 equilibrated at 600 °C (Bernasconi et al., 2018), and Devils Hole, a cave vein calcite precipitated near  
 326 isotopic equilibrium at 33.7 °C (Winograd et al., 1988, 1992; Coplen, 2007). These values were used as  
 327 the AFFs,  $\Delta_{63-47}^*$  and  $\Delta_{64-48}^*$ , for 600 °C and 33.7 °C. Regressions were made for  $\Delta_{63-47}^*$  and  $\Delta_{47}$  and  $\Delta_{64-48}^*$   
 328 and  $\Delta_{48}$ . These regressions (Equations 4 and 5) can be used to calculate acid digestion fractionation  
 329 factors for unknown samples (Lucarelli et al., 2021), and then applied in Equations 6 and 7 to calculate  
 330  $\Delta_{63}$  and  $\Delta_{64}$ .

331

$$332 \Delta_{63-47}^* = 0.0190 \times \Delta_{47 \text{ I-CDES}} + 0.1842 \quad (4)$$

333

$$334 \Delta_{64-48}^* = 0.0077 \times \Delta_{48 \text{ CDES } 90} + 0.1290 \quad (5)$$

335

$$336 \Delta_{63} = \Delta_{47 \text{ I-CDES}} - \Delta_{63-47}^* \quad (6)$$

337

$$338 \Delta_{64} = \Delta_{48 \text{ CDES } 90} - \Delta_{64-48}^* \quad (7)$$

339

340

### 341 3.5 $\Delta_{48}$ mixing model

342

343 For this study, a numerical model was built to estimate  $\Delta_{48}$  mixing effects in  $\text{CaCO}_3$  and was  
344 compared to experimental data for two carbonate reference materials, Mallinckrodt and CM Tile, which  
345 are used as isotopic endmembers. The model was constructed based on methods detailed in Deffliese and  
346 Lohmann et al. (2015), with the addition of  $\delta^{48}$  and  $\Delta_{48}$  in this study. In the model,  $\Delta_{47}$ ,  $\Delta_{48}$ ,  $\delta^{18}\text{O}$ , and  $\delta^{13}\text{C}$   
347 values are assigned to each endmember.  $\delta^{18}\text{O}$  and  $\delta^{13}\text{C}$  values are also given to a hypothetical working gas  
348 (WG). The slope and intercept for an empirical transfer function (ETF) are entered into the model. All  
349 isotopic values for model samples and the working gas, as well as the transfer function values, were based  
350 on experimental data taken from the Nu Perspective instruments. No acid fractionation factor was used,  
351 and model calculations were based on values determined in the I-CDES (Bernasconi et al., 2021)  
352 reference frame at 90 °C. The model calculates  $\delta^{45}$ ,  $\delta^{46}$ ,  $\delta^{47}$ ,  $\delta^{48}$ ,  $\delta^{18}\text{O}$ , and  $\delta^{13}\text{C}$  values of  $\text{CO}_2$  gas  
353 produced by phosphoric acid digestion of carbonate relative to a working gas (WG). The ratio of each  
354 endmember is entered into the model and the isotopic values of the mix are calculated. The full set of  
355 equations and parameters used and a link to a Github site where the model can be downloaded are  
356 detailed in the Appendix (section S.1).

357

### 358 3.6 Parameters used for IsoDIC modelling

359

360 To estimate the evolution of the isotopic composition of  $\text{HCO}_3^-$  and  $\text{CO}_3^{2-}$  endmembers during  
361  $\text{CO}_2$  absorption in an aqueous solution at pH 10.5, in conditions similar to our experiments, we used the  
362 IsoDIC model (Guo, 2020). This numerical modeling software predicts kinetic clumped isotope  
363 fractionations in the DIC- $\text{H}_2\text{O}$ - $\text{CO}_2$  system. The model simulates five key reactions (Reactions 3-7) that  
364 control isotope fractionation, and all related isotopologue reactions involving  $^{12}\text{C}$ ,  $^{13}\text{C}$ ,  $^{16}\text{O}$ ,  $^{17}\text{O}$ , and  $^{18}\text{O}$ ,  
365 for a total of 155 reactions. The forward and reverse rate constants were estimated using equation 8,

366

$$367 k^* = \alpha_{\text{KIE}} \times k \quad (8)$$

368

369 where  $k^*$  is the rate constant of the isotopically substituted reaction,  $k$  is the rate constant of the  
370 isotopically non-substituted reactions, and  $\alpha_{\text{KIE}}$  is the kinetic isotope fractionation factor for the  
371 isotopically substituted reaction. Isotopic equilibrium was assumed between  $\text{HCO}_3^-$  and  $\text{CO}_3^{2-}$  and  $\text{H}_2\text{O}$   
372 and  $\text{OH}^-$  due to rapid equilibration via Reactions 5-7 relative to the reaction rate of hydration (Reaction 1)  
373 and hydroxylation (Reaction 2). Therefore, the only reactions that contribute to isotopic fractionation in  
374 the IsoDIC model are the forward and reverse  $\text{CO}_2$  hydration and hydroxylation reactions (Guo, 2020).

375

376 To use the IsoDIC model in the  $\text{CO}_2$  absorption regime, we assumed the model default values for  
377  $\delta^{13}\text{C}$  of the  $\text{CO}_2$  in air of -10 ‰,  $\delta^{18}\text{O}_{\text{VSMOW}}$  of water to be 0 ‰, and  $\Delta^{17}\text{O}_{\text{VSMOW}}$  of water to be 0 ‰ (Guo,  
378 2020). The initial oxygen and clumped isotope values of DIC and air were set to be in equilibrium with  
379 water. We set the solution temperature to be 5°C in the first simulation and 25°C in the second simulation,  
380 both with a solution pH of 10.5. The model has a total evolution time of 12 hours. The full set of  
381 equations used are available in Guo (2020).

381

### 382 3.7 Box model for kinetic isotope effects in $\Delta_{47}$ , $\Delta_{48}$ , and $\delta^{18}\text{O}$

383

384 To predict kinetic isotope effects in calcite during CO<sub>2</sub> absorption for  $\Delta_{47}$ ,  $\Delta_{48}$ , and  $\delta^{18}\text{O}$ , we used  
 385 a box model built on the ExClump38 framework (Chen et al., 2018; Uchikawa et al., 2021; Watkins and  
 386 Devriendt, 2021). The model tracks the isotopic composition of DIC species in a homogeneous (i.e., well-  
 387 stirred) solution from an initial unequilibrated state. In the box model, the isotopic composition of DIC is  
 388 affected by two additional fluxes: (1) a specified CO<sub>2</sub> influx and (2) a calculated CaCO<sub>3</sub> outflux that is  
 389 based on the following reactions:



394  
 395 These reactions affect the isotopic composition of DIC in two ways: (1) the rate constants for Reactions 8  
 396 and 9 are mass dependent and can therefore influence the isotopic composition of residual DIC (Watkins  
 397 and Hunt, 2015) and (2) the rate of calcite precipitation affects the degree of hydration/hydroxylation  
 398 reaction reversibility at steady state and the extent to which the kinetic isotope effects attending these  
 399 reactions are expressed in solution.

400 In the model, we begin with  $[\text{Ca}^{2+}] = 10$  mM and enough DIC to bring the initial degree of  
 401 supersaturation to 7, as estimated from Dietzel et al. (2009) for spontaneous nucleation of calcite;

402  
 403 
$$\Omega = \frac{[\text{CO}_3^{2-}][\text{Ca}^{2+}]}{K_{sp}(\text{calcite})} \sim 7$$
 (9)

404  
 405 where  $\Omega$  is the saturation state and  $K_{sp}$  is the solubility product for calcite. The DIC is initially isotopically  
 406 equilibrated. As CO<sub>2</sub> fluxes into solution it gets converted to isotopically lighter-than-equilibrium HCO<sub>3</sub><sup>-</sup>  
 407 and CO<sub>3</sub><sup>2-</sup> by hydration (Reaction 3) and hydroxylation (Reaction 4). The rate of calcite growth depends  
 408 on  $[\text{Ca}^{2+}]$  and  $[\text{CO}_3^{2-}]$ , which is updated at each time step. Each simulated experiment lasts 1000 hours,  
 409 which is far longer than the time required to reach steady state, and outputs the steady state composition  
 410 of each DIC species and calcite. In the default scenario, we treat the reaction rate constants as “known”  
 411 and the ion-by-ion model as “correct” to assess how well the model predicts the trends observed in the  
 412 data. This leaves the CO<sub>2</sub> flux ( $F_{\text{CO}_2}$ ) as the only adjustable parameter in the default scenario, but even  
 413  $F_{\text{CO}_2}$  (which is equal to  $F_{\text{CaCO}_3}$  at steady state) is constrained by the data. A description of all equations  
 414 and parameters used are provided in Appendix (S.2) that also contains a link to a Github site with the  
 415 parameters utilized and code used.

416 The steady state  $\Delta_{47}$ ,  $\Delta_{48}$ , and  $1000\ln\alpha_{\text{carb-water}}$  at variable pH from 8.3 to 11, at temperatures  
 417 of 5 °C and 25 °C, and variable FCO<sub>2</sub> (related to calcite growth rate) ranging from typical experimental  
 418 rates to those from extremely slow calcite growth. The oxygen fractionation factor between carbonate and  
 419 water,  $\alpha_{\text{carb-water}}$ , is expressed by the equation:

420  
 421 
$$\alpha_{\text{carb-water}} = \frac{{}^{18}R_{\text{carb}}}{{}^{18}R_{\text{water}}} = \frac{\delta^{18}\text{O}_{\text{carb}}+1000}{\delta^{18}\text{O}_{\text{water}}+1000}$$
 (10)

422  
 423 where  ${}^{18}\text{R}$  is the ratio of  ${}^{18}\text{O}$  to  ${}^{16}\text{O}$  in the carbonate and water.

424 We repeated the same model calculations, but simulated the impact of the addition of 0.25 μM  
 425 CA. All model calculations had 0 ‰ salinity, while experiments had a starting ionic strength of ~0.045

426 mol/L. This should have a negligible effect on our model calculations given that the reaction rate  
427 constants will not be affected by the ionic strength. We compared the results of the model calculations  
428 (with and without CA) to our experimental data (with and without CA) and to experimental data from  
429 Tang et al. (2014), where calcite was precipitated at pH 8.3, 8.5, 9.0, 10.0, and 10.5 at 5 °C, and pH 8.3 at  
430 25 °C (no enzyme was utilized in their experiments).

431

432

## 433 4. Results

434

### 435 4.1 Calcite precipitated with and without carbonic anhydrase

436

#### 437 4.1.1 $\delta^{13}\text{C}$ and $\delta^{18}\text{O}$

438

439 Calcite, verified by XRD, precipitated at increasing pH had an increasing amount of  $\delta^{18}\text{O}$   
440 depletion (Figure 2A-D, Table 3). The largest  $\delta^{18}\text{O}$  depletion relative to the near equilibrium sample  
441 (precipitated at the same temperature at pH 8.3 with CA) was observed in the samples with the lowest  
442 temperature and highest pH, at 5 °C and pH 10.5 and 11.0, with depletions of 17.7 ‰ and 18.8 ‰,  
443 respectively. All samples precipitated with and without CA at pH 8.3 had statistically identical  $\delta^{18}\text{O}$ . At 5  
444 °C, depletions in  $\delta^{18}\text{O}$  were observed at pH > 9. Calcite precipitated without CA had depleted  $\delta^{13}\text{C}$  when  
445 compared to samples precipitated with CA for all temperatures and pHs (Figure 2E-H, Table 3).

446

#### 447 4.1.2 $\Delta_{47}$ and $\Delta_{48}$

448

449 For a given temperature, calcite precipitated with and without CA at pH 8.3 had statistically  
450 identical  $\Delta_{47}$  and  $\Delta_{48}$ . Samples precipitated without CA at pH  $\geq 9.5$  had enriched  $\Delta_{47}$  and depleted  $\Delta_{48}$   
451 values relative to calcite precipitated with CA, and these samples also had negative  $\Delta_{48}$  values (i.e.,  
452  $^{12}\text{C}^{18}\text{O}^{18}\text{O}$  occurring less frequently than predicted due to random chance) (Figure 3, Table 3). The  
453 enrichment of  $\Delta_{47}$  and depletion of  $\Delta_{48}$  increased with increasing pH. The largest  $\Delta_{47}$  enrichment was 0.198  
454 ‰ at 5 °C and pH 10.5. The largest  $\Delta_{48}$  depletion was -0.628 ‰ at 5 °C and pH 11.0. Despite the  
455 relatively large depletions in  $\Delta_{48}$  compared to enrichments in  $\Delta_{47}$ , CA appears to be more effective at  
456 returning  $\Delta_{48}$  values to near-equilibrium values than for  $\Delta_{47}$ .

457 Kinetic slopes for  $\Delta_{47}$  and  $\delta^{18}\text{O}$ ,  $\Delta_{48}$  and  $\delta^{18}\text{O}$ , and  $\Delta_{48}$  and  $\Delta_{47}$  were determined (Table 4). Kinetic  
458 slopes for  $\Delta_{47}$  and  $\delta^{18}\text{O}$  (Figure 4A-D) at 5 °C, 10 °C, 15 °C, and 25 °C were  $-0.011 \pm 0.001$ ,  $-0.013 \pm$   
459  $0.0001$ ,  $-0.012 \pm 0.0002$ , and  $-0.020 \pm 0.001$ , respectively. Kinetic slopes for  $\Delta_{48}$  and  $\delta^{18}\text{O}$  (Figure 4E-H)  
460 at 5 °C, 10 °C, 15 °C, and 25 °C were  $0.033 \pm 0.001$ ,  $0.038 \pm 0.0004$ ,  $0.034$ , and  $0.048 \pm 0.002$ ,  
461 respectively. Kinetic slopes for  $\Delta_{48}$  and  $\Delta_{47}$  (Figure 5) at 5 °C, 10 °C, 15 °C, and 25 °C were  $-2.989 \pm$   
462  $0.125$ ,  $-3.071 \pm 0.011$ ,  $-2.976 \pm 0.034$ , and  $-2.455 \pm 0.024$ , respectively.

463 Equilibrium regressions were made for  $\Delta_{47}$  and  $\Delta_{48}$  relative to precipitation temperature in Kelvin  
464 (Figure 6A-B),  $\Delta_{47}$  and  $\Delta_{48}$  relative to  $\delta^{18}\text{O}$  (Figure 6C-D), and  $\Delta_{48}$  and  $\Delta_{47}$  (Figure 6E), for calcite  
465 precipitated at 5 °C, 10 °C, 15 °C, and 25 °C with CA at pH 8.3, which are expected to achieve quasi-  
466 isotopic equilibrium. Devils Hole core DH-2 data previously analyzed in Lucarelli et al. (2021) was  
467 included in the equilibrium regressions for  $\Delta_{48}$  and  $\Delta_{47}$ ,  $\Delta_{47}$  and precipitation temperature, and  $\Delta_{48}$  and  
468 precipitation temperature. Devils Hole has been shown to be near isotopic equilibrium (Winograd et al.,

469 1998; Coplen, 2007) and has a very precisely known precipitation temperature of  $33.7 \pm 0.2$  °C (Plummer  
470 et al., 2000). The experimental  $\Delta_i$  and  $T$  relationships were determined to be

471  
472  $\Delta_{47 \text{ I-CDES}} = (0.037 \pm 0.002) \times 10^6 T^2 + (0.175 \pm 0.026); r^2 = 0.99$  (10)

473  $\Delta_{48 \text{ CDES 90}} = (0.013 \pm 0.001) \times 10^6 T^2 + (0.100 \pm 0.012); r^2 = 0.98$  (11)

474  
475 where  $T$  is the precipitation temperature in Kelvin. The  $\Delta_{48}$  and  $\Delta_{47}$  relationship is represented by equation  
476 12.

477  
478  $\Delta_{48 \text{ CDES 90}} = (0.355 \pm 0.030) \Delta_{47 \text{ I-CDES}} + (0.039 \pm 0.018); r^2 = 0.98$  (12)

479  
480 The equilibrium relationships for  $\Delta_{47}$  and  $\Delta_{48}$  and  $\delta^{18}\text{O}$  (Figure 6C-D) are represented by equations 13 and  
481 14.

482  
483  $\Delta_{47 \text{ I-CDES}} = (0.013 \pm 0.001) \delta^{18}\text{O}_{\text{VPDB}} + (0.743 \pm 0.006); r^2 = 0.99$  (13)

484  $\Delta_{48 \text{ CDES 90}} = (0.004 \pm 0.001) \delta^{18}\text{O}_{\text{VPDB}} + (0.303 \pm 0.005); r^2 = 0.97$  (14)

485

#### 486 **4.1.3 Measured and modeled $\Delta_{47}$ , $\Delta_{48}$ , $\alpha_{\text{carb-water}}$ , and growth rate effects**

487

488 We compare our calcite isotopic values to those we predicted using the IsoDIC model (Guo,  
489 2020) for different temperatures and pH in Figure 7. We used the model to quantify the temporal  
490 evolution of disequilibrium  $\Delta_{63}$  and  $\Delta_{64}$  in bicarbonate and carbonate ion endmembers during  $\text{CO}_2$   
491 absorption in an aqueous solution at pH 10.5 at 5 °C and 25 °C. The experimental kinetic slope for our  
492 samples precipitated at 5 °C and pH  $\geq 9.5$  was  $m = -3.127 \pm 0.302$  and for samples precipitated at 25 °C at  
493 pH 10.5,  $m = -2.485 \pm 0.025$  (Figure 7). The model trajectories agree with titration data indicating that in  
494 experiments with pH  $\geq 9.5$  at 5 °C and 25 °C, calcite precipitation began during the first day. At both  
495 temperatures, the calcite precipitated at pH 10.5 exceeded the model predictions for maximum enrichment  
496 of  $\Delta_{63}$ , and conversely, did not achieve the maximum amount of depletion for  $\Delta_{64}$  predicted by the model,  
497 that could indicate the influence of another factor, such as growth rate.

498 We compare our experimentally constrained mineral isotopic compositions to box model  
499 calculations that factor into account modulation of isotopic fractionation by growth rate (Figure 8). We  
500 used the model to predict  $1000\ln(\alpha_{\text{carb-water}})$ ,  $\Delta_{47}$ , and  $\Delta_{48}$  with and without CA and compared simulated  
501 values to our experimental results. We also compared our results to experimental data from Tang et al.  
502 (2014) (Figure 8). Tang et al. (2014) performed calcite precipitation experiments at pH 8.3, 8.5, 9.0, 9.5,  
503 10.0, and 10.5 at 5 °C, and pH 8.3 at 25 °C, with precipitation rates ranging from -5.99 to -7.38. Our  
504 precipitation rates are given as the log of  $R$  ( $\text{mol s}^{-1} \text{m}^{-2}$ ) for direct comparability to previous modeling  
505 and measurements (Table 1). The precipitation rates measured here range from -7.02 to -7.48, which are  
506 typical growth rates for calcite precipitation experiments or for corals, which range from  $\sim -4.8$  to  $\sim -7.6$   
507 (Dietzel et al., 2009; Ghosh et al., 2006; Saenger et al., 2012).

508 The default model for  $1000\ln(\alpha_{\text{carb-water}})$  at 5 °C and 25 °C underestimates the observed  
509 experimental fractionations at high pH, even at the fastest precipitation rate. The largest difference  
510 between the model and experimental values is at 5 °C and pH 10.5, with a model predicted  $1000\ln(\alpha_{\text{carb-}}$   
511  $\text{water})$  value of 22.0, and experimental values of 14.8 and 13.1 for this study and Tang et al. (2014),

512 respectively. The default model-predicted values for  $\Delta_{47}$  and  $\Delta_{48}$  had overall good agreement with  
513 experimental values at high and low pH. Model calculations that consider the addition of 0.25  $\mu\text{M}$  CA  
514 had better agreement with experimental data at  $\text{pH} \geq 10$  at 5 °C and 25 °C.

515 Calcite precipitated at high pH with CA (hollow data points in Figures 4, 5, 7, and 13) followed a  
516 different trajectory with a shallower  $\Delta_{47}$  versus  $\Delta_{48}$  slope ( $m = -0.371 \pm 0.107$  at 5 °C;  $m = -0.443$  at 25 °C)  
517 (Figure 5). The shallower slope may be more representative for organisms that have CA in their  
518 calcifying fluid. Increased disequilibrium was observed in  $\Delta_{47}$  relative to  $\Delta_{48}$  in samples at  $\text{pH} \geq 9.5$  with  
519 CA indicating that CA may be better at equilibrating  $m/z$  64 isotopologues than  $m/z$  63 isotopologues.  
520 Since  $m/z$  63 isotopologues contain both  $^{13}\text{C}$  and  $^{18}\text{O}$  it likely takes longer to equilibrate than  $m/z$  64  
521 isotopologues, which contain 2  $^{18}\text{O}$  atoms and no  $^{13}\text{C}$ , due to CA catalyzing O isotope exchange. It has  
522 been shown experimentally that CA discriminates against  $\text{CO}_2$  and  $\text{HCO}_3^-$  that contain  $^{13}\text{C}$  due to slower  
523 rates of diffusion to the enzyme (Paneth and O'Leary, 1985).

524

## 525 4.2 $\Delta_{47}$ and $\Delta_{48}$ mixing experiment and model results

526

527 Two internal carbonate standards, CM Tile and Mallinckrodt, were used as endmembers to  
528 constrain clumped isotope mixing effects because they have large differences in their bulk and clumped  
529 isotope values. Mix 1 (75 % Mallinckrodt, 25 % CM Tile) had  $\Gamma_{47} = 0.106$  ‰ and  $\Gamma_{48} = 0.039$  ‰, Mix 2  
530 (50 % Mallinckrodt, 50 % CM Tile) had  $\Gamma_{47} = 0.107$  and  $\Gamma_{48} = 0.042$ , Mix 3 (25 % Mallinckrodt, 75 %  
531 CM Tile) had  $\Gamma_{47} = 0.014$  ‰ and  $\Gamma_{48} = 0.007$  ‰ (Figure 9A, Table 5). The measured  $\Delta_{47}$  and  $\Delta_{48}$  were  
532 within error of model predicted values, validating the robustness of the model. Table 6 lists all model  
533 parameters.

534 Figure 9B shows  $\Delta_{47}$  and  $\Delta_{48}$  model predictions for modeled calcite formation with differing  
535 clumped and bulk isotopes, differing clumped isotopes and identical bulk isotopes, and identical clumped  
536 isotopes with differing bulk isotopes. The model with a difference of 0.141‰ for  $\Delta_{47}$  and 0.064 ‰ for  $\Delta_{48}$ ,  
537 and 20 ‰ difference in  $\delta^{18}\text{O}$  and  $\delta^{13}\text{C}$  between endmember 1 (E1) and endmember 2 (E2), had  $\Gamma_{47} = 0.029$   
538 ‰ and  $\Gamma_{48} = 0.039$  ‰. These  $\Gamma_{47}$  and  $\Gamma_{48}$  values were smaller than for the endmembers with the same  
539 clumped isotope values and a 20 ‰ difference in  $\delta^{18}\text{O}$  and  $\delta^{13}\text{C}$ , where  $\Gamma_{47} = 0.086$  and  $\Gamma_{48} = 0.073$ . The  
540 endmembers with differing clumped isotope values and the same bulk isotope values mix linearly. For  
541 endmembers with identical clumped isotope values and differing bulk isotope values (Figure 9C-D), the  
542 largest  $\Gamma_{47}$  and  $\Gamma_{48}$  were 0.769 ‰ and 0.660 ‰, respectively, for endmembers with a 30 ‰ difference in  
543  $\delta^{18}\text{O}$  and  $\delta^{13}\text{C}$ . The smallest  $\Gamma_{47}$  and  $\Gamma_{48}$  predicted were 0.021 ‰ and 0.018 ‰, respectively, for  
544 endmembers with a 10 ‰ difference in  $\delta^{18}\text{O}$  and  $\delta^{13}\text{C}$ .

545

546

## 547 5. Discussion

548

### 549 5.1 Comparison of kinetic effects observed in isotopic data with theory

550

#### 551 5.1.1 $\delta^{18}\text{O}$ and $\delta^{13}\text{C}$

552

553 There are multiple factors that may contribute to the observed clumped and bulk kinetic isotope  
554 effects in this study, including  $\text{CO}_2$  hydration and hydroxylation, pH dependent DIC speciation, growth  
555 rate effects, diffusive isotope effects, and precipitation occurring before temperature and pH dependent

556 equilibrium is achieved in the DIC pool. Modeling predicts that hydration should discriminate against  $^{18}\text{O}$   
557 by 14-15 ‰ and  $^{13}\text{C}$  by 19-23 ‰ at 25 °C, while hydroxylation would discriminate against  $^{18}\text{O}$  by 27-30  
558 ‰ and  $^{13}\text{C}$  by 26-31 ‰ at 25 °C (Boettger and Kubicki, 2021). At a pH > ~8.4 hydroxylation starts to  
559 dominate, and at a pH of 10, hydroxylation represents 95% of reactions (McConnaughey, 1989).  
560 Additionally, at equilibrium,  $\delta^{18}\text{O}$  decreases in DIC species in the following order:  $\text{CO}_2 > \text{H}_2\text{CO}_3 > \text{HCO}_3^-$   
561  $> \text{CO}_3^{2-}$  (Uzdowski et al., 1991; Beck et al., 2005), and at pH > 10,  $\text{CO}_3^{2-}$  dominates the DIC composition  
562 (Hill et al., 2014; Tripathi et al., 2015). This is consistent with what we experimentally observed, with  
563 increasing depletion in oxygen isotopes starting in samples precipitated at pH > 9 without CA (Table 3,  
564 Figure 2).

565 The trend observed in  $\delta^{13}\text{C}$  also indicates subtle depletion starting at pH  $\geq 9.5$  for samples  
566 precipitated without CA (Figure 2). For calcite precipitated with CA, there was depletion starting at pH  $\geq$   
567 9. When calcite precipitated with and without CA at the same pH and temperature were directly  
568 compared, there was an offset observed in  $\delta^{13}\text{C}$ , including for samples precipitated at pH 8.3 (Table 3,  
569 Figure 3). This offset may be due to diffusion and the effects of CA on the  $\text{CO}_2$  gradient between the  
570 inner and outer solutions. The enzyme CA makes the hydration reaction more reversible, and thus, the  
571  $[\text{CO}_2]$  in the outer solution could be higher in experiments with CA. If so, this would decrease the  
572  $\text{CO}_2$  gradient between the inner and outer chambers and lead to less diffusive isotopic fractionation. For  
573 samples precipitated without CA in the outer solutions, the  $\text{CO}_2$  diffusing into the outer chamber would  
574 be isotopically lighter, which is consistent with observations. The offset in  $\delta^{13}\text{C}$  between experiments with  
575 and without CA decreases with increasing pH, consistent with the decreasing influence of the CA-  
576 catalyzed hydration reaction with increasing pH.

577 This same effect is not evident in  $\delta^{18}\text{O}$ , with catalyzed and uncatalyzed reactions precipitated at  
578 pH 8.3 and the same temperature having statistically indistinguishable  $\delta^{18}\text{O}$  values (Figure 2). Since CA  
579 catalyzes the pathway for O exchange among DIC to a nearly instantaneous reaction, does not exchange  
580 C among DIC species, and changes the transition state to a more hydroxylation-type reaction, this  
581 potentially explains why the use of CA may alter the  $\delta^{13}\text{C}$ , but not the  $\delta^{18}\text{O}$ , of inorganically precipitated  
582 carbonates.

583

### 584 **5.1.2 Paired clumped isotopes ( $\Delta_{47}$ - $\Delta_{48}$ and $\Delta_{63}$ - $\Delta_{64}$ ) and clumped isotopes with $\delta^{18}\text{O}$**

585

586 Samples grown at elevated pH without CA exhibit enriched  $\Delta_{47}$  and depleted  $\delta^{18}\text{O}$  (Figure 4)  
587 consistent with  $\text{CO}_2$  hydrolysis (Tripathi et al., 2015; Guo, 2020). These samples also exhibit  
588 “hyperstochastic” values for  $\Delta_{48}$  that we hypothesized resulted from a depletion in  $^{12}\text{C}^{18}\text{O}^{18}\text{O}$  produced by  
589 the relative rate kinetics for different  $\text{CO}_2$  isotopologues during hydration and hydroxylation, which we  
590 test by comparing experimental data to model calculations. Our experimental data yield slopes that range  
591 between -2.455 to -3.071 for  $\Delta_{47}$  and  $\Delta_{48}$  (Figure 5), and -2.485 to -3.127 for  $\Delta_{63}$  and  $\Delta_{64}$ . These  
592 experimental data at high pH fall between model-predicted slopes for  $\text{CO}_2$  absorption and high pH  
593 travertines (Figure 10). The IsoDIC model (Guo, 2020) yields predicted slopes for  $\Delta_{63}$  and  $\Delta_{64}$  of  $\text{HCO}_3^-$   
594 produced from hydration and hydroxylation reactions during  $\text{CO}_2$  absorption,  $\text{CO}_2$  outgassing, DIC  
595 speciation, DIC diffusion, thermodynamic equilibrium, and in pH 11.5 travertines. We calculated model-  
596 predicted slopes using the clumped isotope composition of the bicarbonate endmember for times ranging  
597 from 0-5 minutes after the initial reaction occurs. The model predicted slope for  $\Delta_{63}$  and  $\Delta_{64}$  during  $\text{CO}_2$   
598 absorption at a pH 9 was -1.72, while the predicted slope for pH 11.5 travertines was -8.33.

599 We were able to simulate observed hyperstochastic  $\Delta_{64}$  values that are consistent with our  
600 experimental observations of  $\Delta_{48}$ . Our measured kinetic slopes at 25 °C for  $\Delta_{47}$  and  $\delta^{18}\text{O}$  of  $-0.020 \pm 0.001$ ,  
601 and  $\Delta_{48}$  and  $\delta^{18}\text{O}$  of  $0.048 \pm 0.002$  (Figure 5, Table 4) are in good agreement with model predicted slopes

602 for hydration/hydroxylation during CO<sub>2</sub> absorption of -0.024 for  $\Delta_{47}$  and  $\delta^{18}\text{O}$  and 0.041 for  $\Delta_{48}$  and  $\delta^{18}\text{O}$   
603 (Guo, 2020). This agreement indicates that hydration and hydroxylation KIEs occurring following CO<sub>2</sub>  
604 absorption are likely the most significant KIEs observed in our samples precipitated at elevated pH.

605 In our 5 °C sample at pH 9, there was a depletion in  $\delta^{18}\text{O}$  of 4 ‰ relative to the calcite  
606 precipitated with CA under the same conditions, and no statistically significant change in  $\Delta_{47}$  (Table 3).  
607 This may indicate that carbonates precipitated at pH  $\leq 9$  are more likely to exhibit a decoupling of  
608 disequilibrium in  $\delta^{18}\text{O}$  and  $\Delta_{47}$ , but calcite precipitated at pH  $\geq 9.5$  exhibit disequilibrium in  $\delta^{18}\text{O}$  and  $\Delta_{47}$   
609 values. It should also be noted that our 5 °C sample at pH 9 had a depletion of 0.042 ‰ relative to  
610 expected equilibrium in  $\Delta_{48}$ , possibly indicating a greater sensitivity to pH and non-equilibrium oxygen  
611 isotope values than for  $\Delta_{47}$ , potentially due to the presence of two <sup>18</sup>O substitutions in *m/z* 64  
612 isotopologues. It is possible this may represent the same type of decoupling between oxygen isotopes and  
613  $\Delta_{47}$  that were observed in deep-sea corals (Thiagarajan et al., 2011).

614

### 615 *5.1.3 The effect of precipitation rate on bulk and clumped isotopes*

616

617 KIEs resulting in non-equilibrium clumped isotope compositions of DIC species have the  
618 potential to be recorded in carbonate minerals, modulated by growth rate (Tripathi et al., 2015; Watkins  
619 and Hunt, 2015). It has been suggested that at rapid growth rates, a kinetic limit may be reached while at  
620 slow growth, an equilibrium limit may be attained (e.g., DePaolo, 2011; Tripathi et al., 2015; Watkins and  
621 Hunt, 2015). For samples precipitated at pH 8-9 in a solution with a fully equilibrated DIC pool at 25 °C,  
622 Watkins and Hunt (2015) used an ion-by-ion growth model to predict that the  $\Delta_{63}$  of calcite precipitated at  
623 typical experimental growth rates ( $\log_{10}R = -5$  to  $-7$  mol/m<sup>2</sup>/s) should be at or near the kinetic limit, and  
624 that given equilibrium isotopic compositions for DIC endmembers (Hill et al., 2014; Tripathi et al., 2015),  
625 calcite  $\Delta_{63}$  would be  $\sim 0.01$  ‰ higher than expected equilibrium value at 25 °C, while for samples  
626 precipitated at pH  $> 10$ , calcite would be  $\sim 0.01$  ‰ to  $\sim 0.02$  ‰ lower than expected equilibrium  $\Delta_{63}$   
627 values. The kinetic limit should be substantially different if the DIC pool has not achieved equilibrium  
628 (Tripathi et al., 2015; Guo, 2020), and we find that our measured  $\Delta_{47}$  values for samples precipitated at pH  
629 10.5 have  $\Delta_{47}$  that are elevated by 0.168-0.198 from expected mineral equilibrium values (Figure 3).  
630 While these observations are consistent with relatively large kinetic effects associated with CO<sub>2</sub>  
631 absorption, including hydration, hydroxylation, and a DIC pool that is not equilibrated, it is also likely  
632 they include a kinetic contribution to the isotopic signatures from growth rate effects.

633 For samples from this study and most from Tang et al. (2014) at pH 8.3, we find that  $\Delta_{47}$  and  $\Delta_{48}$   
634 values are indistinguishable from equilibrium values irrespective of precipitation rate. This is the case for  
635 calcite precipitation at temperatures of 5 °C and 25 °C, both with and without CA. This suggests that the  
636 intrinsic kinetic fractionation factor for clumped isotopes is close to unity (Guo, 2020) and that accurate  
637 temperatures can be retrieved even when there are large kinetic oxygen isotope effects.

638 At higher pH, over the growth rates observed here, modeling and experimental data suggests that  
639 mineral disequilibrium occurs. Specifically, our calculations (Figure 8) suggest that samples precipitated  
640 at the same pH and temperature but at different growth rates, in a system where CO<sub>2</sub> absorption is  
641 dominant, and a DIC pool that has not reached equilibrium, may yield calcite with mineral disequilibrium  
642 of up to  $\sim 8.4$  for  $1000\ln(\text{carb-water})$ ,  $\sim 0.23$  ‰ for  $\Delta_{47}$ , and  $\sim 0.51$  ‰ for  $\Delta_{48}$ . These effects are the largest  
643 for calcite growing at pH  $\geq 9.5$  and low temperature.

644 We note this model underestimates oxygen isotope fractionations observed in the experimental  
645 samples synthesized in both this study and Tang et al. (2014) at multiple temperature and pH. This may

646 reflect the presence of an additional KIE influencing oxygen isotopes in DIC. In both this work and in  
647 Tang et al. (2014), CO<sub>2</sub> diffused through a polyethylene membrane, which may enrich the solution in <sup>12</sup>C  
648 and <sup>16</sup>O. Thus, results may reflect a kinetic oxygen isotope effect from membrane diffusion, as Tang et al.  
649 (2014) hypothesized in their work. Since the time to reach isotopic equilibrium is much longer at high pH  
650 and low temperature (Beck et al., 2005), a diffusive signal in oxygen isotopes would be more apparent in  
651 samples precipitated at high pH and low temperature, which is what we observe. The other possibility is  
652 that the hydroxylation KFFs from the literature are underestimated. When the hydroxylation KFF for  
653 oxygen is increased to match the 1000ln( $\alpha_{\text{carb-water}}$ ) data (Figure 8Q-X), however, there is significantly less  
654 agreement between measured and modeled  $\Delta_{48}$ . This suggests either that diffusion is responsible for the  
655 low 1000ln( $\alpha_{\text{carb-water}}$ ) values or that the model is over-predicting the sensitivity of  $\Delta_{48}$  to kinetic oxygen  
656 isotope fractionations. Additionally, the model may underestimate the catalytic ability of CA to  
657 equilibrate  $\Delta_{47}$  and  $\Delta_{48}$  for calcite formed at fast growth rates and at high pH.

658 However, no such signal is observed for clumped isotopes, with all measured sample  $\Delta_{47}$  and  $\Delta_{48}$   
659 values residing within the model predicted range, with the exception of one calcite sample precipitated  
660 with CA at pH 11 at 25°C. It may be possible that a diffusive signal, which is expected to lower  $\delta^{18}\text{O}$  and  
661 increase  $\Delta_{47}$  (Thagarajan et al., 2011), is smaller or absent in the experimental  $\Delta_{47}$  and  $\Delta_{48}$ . Currently, we  
662 are unable to resolve the diffusive contribution to our experimental isotope signatures, but an upper bound  
663 of a 22 ‰ decrease for  $\delta^{18}\text{O}$  and 0.5 ‰ increase for  $\Delta_{47}$  for Knudsen diffusion was calculated by Eiler and  
664 Schauble (2004). An additional possibility is that the oxygen isotope kinetic fractionation factors used in  
665 the model calculations are underestimated. However, when oxygen isotope kinetic fractionation factors  
666 are increased to match experimental oxygen isotope data (Figure 8Q-X) the agreement between model  
667 and experimental  $\Delta_{48}$  is decreased. This may indicate that another kinetic effect is the source of the  
668 mismatch between modeled and measured 1000ln( $\alpha_{\text{carb-water}}$ ) or that  $\Delta_{48}$  is less sensitive to oxygen isotope  
669 fractionation factors than is predicted by the model.

670 Future work could further constrain growth rate effects by precipitating calcite under controlled  
671 conditions over an even broader range of growth rates than what was done in this work and in Tang et al.  
672 (2014). This would allow for experimental data to be compared to model predictions for the slow and fast  
673 growth limits. Diffusion effects could also be explored by precipitating calcite at fast growth rates from  
674 CO<sub>2</sub> diffused at different rates through membranes of varying pore sizes.

675

## 676 **5.2 Paired clumped isotope data: Near equilibrium mineral compositions**

677

678 Samples grown at pH 8.3 and at variable temperatures with CA yield  $\Delta_{47}$  and  $\Delta_{48}$  values that are  
679 consistent with mineral equilibrium as constrained using multiple independent approaches. The calcite  
680 growth rates achieved are ones that our modeling indicates should attain the equilibrium limit, and  
681 experimental data and model calculations converge (Figure 8). Theory from Hill et al. (2014) and Tripathi  
682 et al. (2015) combined with experimental AFF values (Lucarelli et al., 2021) show that measured  $\Delta_{47}$  and  
683  $\Delta_{48}$  from this work are consistent with calcite equilibrium (Figure 11A-C).

684 These results lend further support to experimental and field-derived calibration datasets being in  
685 near equilibrium. An F test (performed in PRISM 7) was used for a statistical comparison between  
686 experimentally determined regressions for  $\Delta_{47}$  and  $\Delta_{48}$  values for near-equilibrium samples with known  
687 precipitation temperatures from Swart et al. (2021), Fiebig et al. (2021), with results from this study  
688 (Table 7). The test determined that the regressions were not statistically different ( $p = 0.99$ , Table 8) and a  
689 combined regression is represented by equation 15 (Figure 11).

690

$$\Delta_{48 \text{ CDES } 90} = (0.407 \pm 0.016) \Delta_{47 \text{ CDES } 90} + (0.006 \pm 0.009); r^2 = 0.98 \quad (15)$$

692

693 The data from Fiebig et al. (2021) includes lake and cave calcites, inorganic precipitations, and samples  
694 equilibrated at high temperatures, with samples having crystallization temperatures from 7.9 °C to 1100  
695 °C. Sample data from Swart et al. (2021) includes 7 inorganic calcite precipitations from 5 °C to 65 °C.  
696 The experimentally determined regressions from Swart et al. (2021), Fiebig et al. (2021), and this study  
697 are bracketed by regressions from Bajnai et al. (2020) and Lucarelli et al. (2021) determined using a  
698 combination of theory from Hill et al. (2014) and Tripathi et al. (2015) and experimental AFF values.  
699 These regressions are statistically indistinguishable from the experimental regressions ( $p = 0.99$ ).

700

701 It was also determined that the experimental regressions based on samples with known  
702 precipitation temperatures from Swart et al. (2021), Fiebig et al. (2021), and this study are statistically  
703 indistinguishable ( $p > 0.99$ ) from the  $\Delta_{47}$  and  $\Delta_{48}$  regression from Lucarelli et al. (2021) based on  
704 measurements of 20 carbonates, most of which are used as standards and had unknown precipitation  
705 temperatures but were shown to have clumped isotope values near clumped isotopic equilibrium. The  
706 combined regression for these experimental datasets is represented by equation 16.

707

$$\Delta_{48 \text{ CDES } 90} = (0.429 \pm 0.010) \Delta_{47 \text{ CDES } 90} - (0.006 \pm 0.006); r^2 = 0.98 \quad (16)$$

708

709 An F test was used to test for statistical differences between experimentally determined  
710 regressions for  $\Delta_{47}$  and  $10^6 T^{-2}$  and  $\Delta_{48}$  and  $10^6 T^{-2}$  from Swart et al. (2021), Fiebig et al. (2021), and this  
711 study (Figure 11). It was determined that these regressions were not statistically different ( $p = 0.99$  for  $\Delta_{47}$   
712 and  $10^6 T^{-2}$ ;  $p = 0.99$  for  $\Delta_{48}$  and  $10^6 T^{-2}$ ). The combined experimentally based regressions are presented in  
713 equations 17 and 18 with temperature in Kelvin.

714

$$\Delta_{47 \text{ I-CDES}} = (0.037 \pm 0.001) \times 10^6 T^{-2} + (0.178 \pm 0.009); r^2 = 0.99 \quad (17)$$

715

$$\Delta_{48 \text{ CDES } 90} = (0.015 \pm 0.0005) \times 10^6 T^{-2} + (0.078 \pm 0.006); r^2 = 0.98 \quad (18)$$

717

718 The experimental regressions were also determined to be statistically indistinguishable from the  
719 regressions based on theory and experimental AFFs from Bajnai et al. (2020) and Lucarelli et al. (2021)  
720 ( $p = 0.99$ ).

721

722 Offsets in  $\Delta_{48}$  are likely from differences in standardization. This study and Lucarelli et al. (2021)  
723 used carbonate-based standardization, Swart et al. (2021) used gas-based standardization, and Bajnai et al.  
724 (2020) and Fiebig et al. (2021) used a combination of carbonate and gas-based standardization. For  $\Delta_{47}$ ,  
725 this study and Fiebig et al. (2021) use the I-CDES reference frame, while Bajnai et al. (2020) and Fiebig  
726 et al. (2021) use the CDES 90 reference frame. While I-CDES and CDES 90 are very similar reference  
727 frames being that they are both present data at 90 °C, the main difference is that the I-CDES reference  
728 frame uses multi-lab determined values presented in Bernasconi et al. (2021) for the carbonate standards  
729 ETH-1, ETH-2, and ETH-3 for standardization, while CDES 90 may use slightly different values these  
730 carbonate standards and other carbonate standards or may also present data relative to equilibrated gas  
731 standards. All data reported thus far use the CDES 90 reference frame for  $\Delta_{48}$ , however, differences in  
732 values used for carbonate standards and the use of carbonate and/or gas-based standardization vary  
733 between labs, as discussed in Lucarelli et al. (2021). Additionally,  $\Delta_{48}$  is relatively sensitive compared to  
 $\Delta_{47}$  to subtle changes in transfer functions and nonlinearity slopes used in data corrections. For example, a

734 shift of  $\sim 0.05$  in the slope of the  $\Delta_{48}$  transfer function can shift  $\Delta_{48}$  values by  $\sim 0.029$  ‰, while the same  
735 magnitude shift in the  $\Delta_{47}$  transfer function will shift  $\Delta_{47}$  values by  $\sim 0.013$  ‰ (Supplementary Table S5).  
736

### 737 **5.3 Mixing effects in paired clumped isotopes**

738  
739 Biominerals and abiotic natural systems often have fluxes of isotopically distinct fluids associated  
740 with carbonate mineral precipitation, which in turn can yield products with distinct bulk isotopic  
741 compositions. This can occur from the precipitation processes themselves, or arise from temperature  
742 fluctuations over the course of precipitation, or be associated with the integration of seawater into  
743 calcifying spaces. Additionally, diagenetic processes can give rise to multiple phases of carbonates being  
744 present, which in turn can be sampled. Thus, it is possible that carbonates with different bulk isotopic  
745 compositions, and clumped isotope compositions, can be mixed physically within a single clumped  
746 isotope sample. Mixing effects have been explored for  $\Delta_{47}$  in  $\text{CO}_2$  (Eiler and Schauble, 2004) and in  
747 carbonate minerals (Defliese and Lohmann, 2015). For carbonate minerals, this can potentially lead to the  
748 underestimation of temperature from enriched  $\Delta_{47}$  values (Defliese and Lohmann, 2015).

749 Both experimental data and theoretical calculations from our non-linear mixing model indicate  
750 that artifacts in both  $\Delta_{47}$  and  $\Delta_{48}$  can arise from mixing (Figures 9-10; Table 6). Values for  $\Delta_{47}$  and  $\Delta_{48}$  in  
751 mixtures are enriched compared to equilibrium values. The trajectories for  $\Delta_{47}$  and  $\Delta_{48}$  mixing effects in  
752 this study have slopes that vary depending on endmember compositions and the fraction of the mixture.  
753 Values for slopes range from 0.397-0.872.

754 For the calculations performed here, the minimum non-linear mixing-related biases occur when  
755 calcite endmembers have the same clumped isotope compositions but a 10 ‰ difference in  $\delta^{18}\text{O}$  and  $\delta^{13}\text{C}$ .  
756 This could represent several scenarios, such as correspond to mixing of carbonate from growth bands in a  
757 coral that formed at the same temperature but with variable bulk compositions, or mixing of different  
758 mollusk specimens that formed at similar temperatures and are within the same sediment sample, or of  
759 adjacent foraminiferal samples during times when temperatures were relatively similar.

760 Maximum mixing-related biases are predicted when calcites with the same clumped isotope  
761 values is mixed that has a 60 ‰ difference in  $\delta^{18}\text{O}$  and  $\delta^{13}\text{C}$  (Figure 9C-D). This type of difference is  
762 likely to rarely be important for most natural settings, though this suggests that caution should be taken  
763 when working with methane-derived carbonates, or when sampling rocks containing cements formed  
764 from brine and freshwater settings.

765 Mixing of samples with different clumped and bulk isotope endmember values predicted from  
766 our model fall between the minimum and maximum trajectories (Figure 9A-B). Our measured values  
767 from mixing experiments fall in this category and agree with model predictions. The minimum trajectory  
768 observed here is slightly higher than the equilibrium slope for  $\Delta_{47}$  and  $\Delta_{48}$ .

769 If endmembers vary by less than 5 ‰ in  $\delta^{13}\text{C}$  and  $\delta^{18}\text{O}$ , mixing effects of 0.005 ‰ could be  
770 observed in  $\Delta_{47}$  and 0.004 ‰ in  $\Delta_{48}$ , which are within the range of instrumental precision. Thus, mixing  
771 could introduce  $\sim 1.9$  °C of potential bias in  $\Delta_{47}$ -derived temperatures (as has previously been discussed in  
772 Defliese and Lohmann, 2015), and  $\sim 3.5$  °C in  $\Delta_{48}$ -derived temperatures, at Earth surface temperatures. If  
773 endmembers have the same bulk composition but varying  $\Delta_{47}$  and  $\Delta_{48}$ , the clumped isotope values mix  
774 linearly as a weighted sum of the contribution of each endmember. Additionally,  $\Delta_{47}$  values below  
775 equilibrium values are predicted when an endmember has  $\delta^{18}\text{O}$  that is higher and  $\delta^{13}\text{C}$  that is lower than  
776 the other endmember. For example, if two endmembers have identical  $\Delta_{47}$ , and one end member has a  
777  $\delta^{18}\text{O}$  of 5 ‰ higher and  $\delta^{13}\text{C}$  of 5 ‰ lower than the other endmember, the resultant  $\Delta_{47}$  value will be

778 0.005 ‰ below the  $\Delta_{47}$  value of each individual endmember. In this scenario, the  $\Delta_{47}$  value continues to  
779 decrease with increasing  $\delta^{18}\text{O}$  and decreasing  $\delta^{13}\text{C}$ .

780 This work indicates that paired clumped isotopes ( $\Delta_{47}$  and  $\Delta_{48}$ ) could be used to identify mixing  
781 effects that would otherwise bias paleothermometry, but also suggests that endmember compositions in  
782 clumped or bulk compositions, or both, would need to be substantially different for biases to be  
783 expressed.  $\Delta_{47}$  and  $\Delta_{48}$  values for unknown calcite samples that do not conform to temperature-dependent  
784 equilibrium  $\Delta_{47}$  -  $\Delta_{48}$  relationship (Figure 11), or kinetically governed disequilibrium mineral signatures  
785 (Figure 10), but that do fall within the mixing effect bounds shown in Figure 10 for calcite samples, could  
786 be indicative of enriched clumped isotope values from non-linear mixing effects. If mixing fractions and  
787 endmembers could be constrained, paired  $\Delta_{47}$  and  $\Delta_{48}$  data could potentially be used to correct for artifacts  
788 and extract primary temperatures.

789

## 790 6. Conclusions

791

792 Utilizing a combination of experimental data and multiple modeling frameworks, we show that  
793 paired  $\Delta_{47}$  and  $\Delta_{48}$  can be used to identify when disequilibrium effects are negligible, and in cases where  
794 disequilibrium is non-negligible, constrain kinetic isotope effects and mixing effects. By precipitating  
795 calcite at five temperatures at pH 8.3 with the enzyme carbonic anhydrase (CA), we reduce kinetic  
796 isotope effects in the DIC pool, with  $\Delta_{47}$  and  $\Delta_{48}$  values consistent with model predictions for equilibrium  
797 precipitation. Experimental data provide an independent set of constraints on the equilibrium relationship  
798 between  $\Delta_{47}$  and  $\Delta_{48}$ ,  $\Delta_{47}$  and  $T$ ,  $\Delta_{48}$  and  $T$ ,  $\Delta_{47}$  and  $\delta^{18}\text{O}$ , and  $\Delta_{48}$  and  $\delta^{18}\text{O}$ . The experimentally determined  
799  $\Delta_{47}$  and  $\Delta_{48}$  relationship from this study is statistically indistinguishable from published regressions. We  
800 report a new combined regression fit through all experimental data from Swart et al. (2021), Fiebig et al.  
801 (2021), Lucarelli et al. (2021), and this study:

802

$$803 \Delta_{48}^{\text{CDES } 90} = (0.429 \pm 0.010) \Delta_{47}^{\text{CDES } 90} - (0.006 \pm 0.006); r^2 = 0.98$$

804

805 which further constrains the equilibrium relationships between  $\Delta_{47}$  and  $\Delta_{48}$ . We also report combined  
806 temperature dependent relationships using data from Swart et al. (2021), Fiebig et al. (2021), and this  
807 study:

808

$$809 \Delta_{47}^{\text{I-CDES}} = (0.037 \pm 0.001) \times 10^6 T^{-2} + (0.178 \pm 0.009); r^2 = 0.99$$

$$810 \Delta_{48}^{\text{CDES } 90} = (0.015 \pm 0.0005) \times 10^6 T^{-2} + (0.078 \pm 0.006); r^2 = 0.98$$

811

812 which further constrains equilibrium relationships between  $\Delta_{47}$  and  $T$ , and  $\Delta_{48}$  and  $T$ .

813 At elevated pH, we observe  $\Delta_{47}$  values that are enriched relative to expected isotope equilibrium,  
814 while  $\Delta_{48}$ ,  $\delta^{18}\text{O}$ , and  $\delta^{13}\text{C}$  are depleted. The largest enrichment relative to quasi-equilibrium observed here  
815 for  $\Delta_{47}$  was 0.198 ‰ at pH 10.5 and 5 °C. The largest depletion relative to quasi-equilibrium for  $\Delta_{48}$  was -  
816 0.628 ‰ at pH 11 and 5 °C. All calcite precipitated here with pH  $\geq$  9.5 had  $\Delta_{48}$  values less than 0 ‰,  
817 indicating values below a stochastic distribution. Calcite precipitated with CA in the solution returned to  
818  $\Delta_{47}$  and  $\Delta_{48}$  values expected at quasi-equilibrium, where CA was more successful at catalyzing  $\Delta_{48}$  than  
819  $\Delta_{47}$ .

820 The kinetic slopes for hydration and hydroxylation for paired  $\Delta_{47}$  and  $\Delta_{48}$  measurements  
821 determined here may be used to return calcite samples to near equilibrium clumped isotope values.  
822 Calcite precipitated at  $\text{pH} \geq 9.5$  followed a steep kinetic slope, while calcite precipitated at  $\text{pH} \geq 9.5$  with  
823 CA followed a shallower kinetic slope. Calcite precipitated at  $\text{pH} \leq 9.0$  had negligible clumped isotope  
824 kinetic effects, while kinetic oxygen isotope effects may have been present.

825 Samples grown at  $\text{pH} 8.3$  and with growth rates of  $\log_{10}R$  that are  $-7.3$  to  $7.5$   $\text{mol/m}^2/\text{s}$  have  $\Delta_{47}$   
826 and  $\Delta_{48}$  values that overlap the equilibrium limit, while samples at higher  $\text{pH}$  have clumped isotope  
827 compositions that record kinetic isotope effects. The observed paired clumped isotope values in calcite  
828 samples grown at elevated  $\text{pH}$  without CA can be explained by hydration/hydroxylation during  $\text{CO}_2$   
829 absorption. Calcite precipitated at fast growth rates may inherit larger kinetic isotopic effects from  $\text{CO}_2$   
830 hydration/hydroxylation and a disequilibrium DIC pool compared to calcite precipitated at slower growth  
831 rates. Kinetic isotope effects associated with fast growth rate and  $\text{CO}_2$  hydration/hydroxylation may be as  
832 large as  $\sim 0.23$  ‰ for  $\Delta_{47}$  and  $\sim 0.51$  ‰ for  $\Delta_{48}$ .

833 Mixing experiments and non-linear mixing model calculations show that mixing results in  
834 enrichments in both  $\Delta_{47}$  and  $\Delta_{48}$  compared to equilibrium values. There are a range of characteristic  
835 trajectories for mixing effects in  $\Delta_{47}$  and  $\Delta_{48}$  for calcites with varying bulk and clumped isotopes. Paired  
836 measurements of  $\Delta_{47}$  and  $\Delta_{48}$  may provide a mechanism by which mixing effects can be identified in  
837 biological and abiogenic carbonate samples. Such effects are likely to be  $\geq 0.009$  ‰ for  $\Delta_{47}$  if there is  
838 more than 30 % of a secondary component in a two-component system if bulk compositions vary by more  
839 than 7 ‰, or if  $\Delta_{47}$  and  $\Delta_{48}$  vary by more than 0.03 ‰.

840

#### 841 **Acknowledgments**

842 We thank lab members past and present for their work running standards, efforts in data entry, and  
843 contributions to discussions, NAWI Graz Central Lab for Water, Minerals and Rocks for experimental  
844 and analytical support, and Albrecht Leis (JR-AquaConSol, Graz) for support on liquid isotope analyses.  
845 This work was funded by DOE BES grant DE-FG02-83613ER16402 to Aradhna Tripathi. Jamie Lucarelli  
846 and Zeeshan Parvez also acknowledge support from fellowships granted by The Center for Diverse  
847 Leadership in Science supported by the Packard Foundation, Sloan Foundation, Silicon Valley  
848 Community Foundation, and NSF (ICER- 2039462 for Veterans in Green STEM). Jamie Lucarelli  
849 received support from Cota Robles and Dissertation Year Fellowships from the University of California,  
850 Los Angeles, and Zeeshan Parvez received support as a Tillman Scholar. We thank Ben Elliot and  
851 members of the Tripathi lab for their technical support in mass spectrometry.

852

#### 853 **Author Contributions**

854 AT initiated and supported the work. AT, MD, BP, and JL designed the research. BP carried out the  
855 precipitation experiments with input from MD and JL. JL performed the isotope analyses and calculations  
856 with input from AT. JL performed the mixing experiments and associated calculations with input from  
857 AT. ZP contributed to the box model and IsoDIC calculations. JW provided the box model script. JL, BP,  
858 RE, MD, and AT contributed insights to data analyses and interpretations. JL wrote the manuscript with  
859 guidance from AT and input from all coauthors. AT and RE advised JL and ZP.

860

#### 861 **References**

862 Adkins, J.F., Boyle, E.A., Curry, W.B. and Lutringer, A., 2003. Stable isotopes in deep-sea corals and a  
863 new mechanism for “vital effects”. *Geochimica et Cosmochimica Acta*, 67(6), pp.1129-1143.  
864 [https://doi.org/10.1016/S0016-7037\(02\)01203-6](https://doi.org/10.1016/S0016-7037(02)01203-6)

865 Affek, H.P., Bar-Matthews, M., Ayalon, A., Matthews, A., Eiler, J.M., 2008. Glacial/interglacial  
866 temperature variations in Soreq cave speleothems as recorded by ‘clumped isotope’ thermometry.  
867 *Geochimica et Cosmochimica Acta* 72, 5351–5360. <https://doi.org/10.1016/j.gca.2008.06.031>

868 Al-Horani, F.A., Al-Moghrabi, S.M., de Beer, D., 2003. Microsensor study of photosynthesis and  
869 calcification in the scleractinian coral, *Galaxea fascicularis*: active internal carbon cycle. *Journal*  
870 *of Experimental Marine Biology and Ecology* 288, 1–15. [https://doi.org/10.1016/S0022-](https://doi.org/10.1016/S0022-0981(02)00578-6)  
871 [0981\(02\)00578-6](https://doi.org/10.1016/S0022-0981(02)00578-6)

872 Anagnostou, E., K-F. Huang, C-F. You, E. L. Sikes, and R. M. Sherrell. "Evaluation of boron isotope  
873 ratio as a pH proxy in the deep sea coral *Desmophyllum dianthus*: Evidence of physiological pH  
874 adjustment." *Earth and Planetary Science Letters* 349 (2012): 251-260.  
875 <https://doi.org/10.1016/j.epsl.2012.07.006>

876 Bajnai, D., Guo, W., Spötl, C., Coplen, T.B., Methner, K., Löffler, N., Krsnik, E., Gischler, E., Hansen,  
877 M., Henkel, D. and Price, G.D., 2020. Dual clumped isotope thermometry resolves kinetic biases  
878 in carbonate formation temperatures. *Nature communications*, 11(1), pp.1-9.  
879 <https://doi.org/10.1038/s41467-020-17501-0>

880 Beck, W.C., Grossman, E.L., Morse, J.W., 2005. Experimental studies of oxygen isotope fractionation in  
881 the carbonic acid system at 15°, 25°, and 40°C. *Geochimica et Cosmochimica Acta* 69, 3493–  
882 3503. <https://doi.org/10.1016/j.gca.2005.02.003>

883 Berg, J., Tymoczko, J., Stryer, L., 2002. *Biochemistry*, 5th ed. W H Freeman, New York.

884 Bernasconi, S.M., Daëron, M., Bergmann, K.D., Bonifacie, M., Meckler, A.N., Affek, H.P., Anderson,  
885 N., Bajnai, D., Barkan, E., Beverly, E. and Blamart, D., 2021. InterCarb: A community effort to  
886 improve interlaboratory standardization of the carbonate clumped isotope thermometer using  
887 carbonate standards. *Geochemistry, Geophysics, Geosystems*, 22(5), p.e2020GC009588.  
888 <https://doi.org/10.1029/2020GC009588>

889 Bernasconi, S.M., Müller, I.A., Bergmann, K.D., Breitenbach, S.F., Fernandez, A., Hodell, D.A., Jaggi,  
890 M., Meckler, A.N., Millan, I. and Ziegler, M., 2018. Reducing uncertainties in carbonate clumped  
891 isotope analysis through consistent carbonate-based standardization. *Geochemistry, Geophysics,*  
892 *Geosystems*, 19(9), pp.2895-2914. <https://doi.org/10.1029/2017GC007385>

893 Bertucci, A., Innocenti, A., Scozzafava, A., Tambutté, S., Zoccola, D., Supuran, C.T., 2011. Carbonic  
894 anhydrase inhibitors. Inhibition studies with anions and sulfonamides of a new cytosolic enzyme  
895 from the scleractinian coral *Stylophora pistillata*. *Bioorganic & Medicinal Chemistry Letters* 21,  
896 710–714. <https://doi.org/10.1016/j.bmcl.2010.11.124>

897 Boettger, J.D., Kubicki, J.D., 2021. Equilibrium and kinetic isotopic fractionation in the CO<sub>2</sub> hydration  
898 and hydroxylation reactions: Analysis of the role of hydrogen-bonding via quantum mechanical  
899 calculations. *Geochimica et Cosmochimica Acta* 292, 37–63.  
900 <https://doi.org/10.1016/j.gca.2020.09.019>

901 Brand, W.A., Assonov, S.S., Coplen, T.B., 2010. Correction for the <sup>17</sup>O interference in δ(<sup>13</sup>C)  
902 measurements when analyzing CO<sub>2</sub> with stable isotope mass spectrometry (IUPAC Technical  
903 Report). *Pure and Applied Chemistry* 82, 1719–1733. [https://doi.org/10.1351/PAC-REP-09-01-](https://doi.org/10.1351/PAC-REP-09-01-05)  
904 [05](https://doi.org/10.1351/PAC-REP-09-01-05)

905 Christensen, J.N., Watkins, J.M., Devriendt, L.S., DePaolo, D.J., Conrad, M.E., Voltolini, M., Yang, W.,  
906 Dong, W., 2021. Isotopic fractionation accompanying CO<sub>2</sub> hydroxylation and carbonate

907 precipitation from high pH waters at The Cedars, California, USA. *Geochimica et Cosmochimica*  
908 *Acta* 301, 91–115. <https://doi.org/10.1016/j.gca.2021.01.003>

909 Coplen, T.B., 2007. Calibration of the calcite–water oxygen-isotope geothermometer at Devils Hole,  
910 Nevada, a natural laboratory. *Geochimica et Cosmochimica Acta* 71, 3948–3957.  
911 <https://doi.org/10.1016/j.gca.2007.05.028>

912 Daëron, M., Blamart, D., Peral, M., Affek, H.P., 2016. Absolute isotopic abundance ratios and the  
913 accuracy of  $\Delta 47$  measurements. *Chemical Geology* 442, 83–96.  
914 <https://doi.org/10.1016/j.chemgeo.2016.08.014>

915 Daëron, M., Drysdale, R.N., Peral, M., Huyghe, D., Blamart, D., Coplen, T.B., Lartaud, F. and Zanchetta,  
916 G., 2019. Most Earth-surface calcites precipitate out of isotopic equilibrium. *Nature*  
917 *communications*, 10(1), pp.1-7. <https://doi.org/10.1038/s41467-019-08336-5>

918 Daëron, M., Guo, W., Eiler, J., Genty, D., Blamart, D., Boch, R., Drysdale, R., Maire, R., Wainer, K.,  
919 Zanchetta, G., 2011.  $^{13}\text{C}^{18}\text{O}$  clumping in speleothems: Observations from natural caves and  
920 precipitation experiments. *Geochimica et Cosmochimica Acta* 75, 3303–3317.  
921 <https://doi.org/10.1016/j.gca.2010.10.032>

922 de Goeyse, S., Webb, A.E., Reichart, G.-J., de Nooijer, L.J., 2021. Carbonic anhydrase is involved in  
923 calcification by the benthic foraminifer *Amphistegina lessonii*; *Biogeosciences* 18, 393–401.  
924 <https://doi.org/10.5194/bg-18-393-2021>

925 Defliese, W.F., Lohmann, K.C., 2015. Non-linear mixing effects on mass-47  $\text{CO}_2$  clumped isotope  
926 thermometry: Patterns and implications: Non-linear mixing effects on mass-47 clumped isotopes.  
927 *Rapid Commun. Mass Spectrom.* 29, 901–909. <https://doi.org/10.1002/rcm.7175>

928 Dennis, K.J., Affek, H.P., Passey, B.H., Schrag, D.P., Eiler, J.M., 2011. Defining an absolute reference  
929 frame for ‘clumped’ isotope studies of  $\text{CO}_2$ . *Geochimica et Cosmochimica Acta* 75, 7117–7131.  
930 <https://doi.org/10.1016/j.gca.2011.09.025>

931 Dietzel, M., Gussone, N., Eisenhauer, A., 2004. Co-precipitation of  $\text{Sr}^{2+}$  and  $\text{Ba}^{2+}$  with aragonite by  
932 membrane diffusion of  $\text{CO}_2$  between 10 and 50 °C. *Chemical Geology* 203, 139–151.  
933 <https://doi.org/10.1016/j.chemgeo.2003.09.008>

934 Dietzel, M., Tang, J., Leis, A., & Köhler, S. J., 2009. Oxygen isotopic fractionation during inorganic  
935 calcite precipitation—Effects of temperature, precipitation rate and pH. *Chemical Geology* 268,  
936 107-115. <https://doi.org/10.1016/j.chemgeo.2009.07.015>

937 Eiler, J.M., Schauble, E., 2004.  $^{18}\text{O}^{13}\text{C}^{16}\text{O}$  in Earth’s atmosphere. *Geochimica et Cosmochimica Acta*  
938 68, 4767–4777. <https://doi.org/10.1016/j.gca.2004.05.035>

939 Fiebig, J., Bajnai, D., Löffler, N., Methner, K., Krsnik, E., Mulch, A., Hofmann, S., 2019. Combined  
940 high-precision  $\Delta 48$  and  $\Delta 47$  analysis of carbonates. *Chemical Geology* 522, 186–191.  
941 <https://doi.org/10.1016/j.chemgeo.2019.05.019>

942 Fiebig, J., Daëron, M., Bernecker, M., Guo, W., Schneider, G., Boch, R., Bernasconi, S.M., Jautzy, J.,  
943 Dietzel, M., 2021. Calibration of the dual clumped isotope thermometer for carbonates.  
944 *Geochimica et Cosmochimica Acta* S0016703721004208.  
945 <https://doi.org/10.1016/j.gca.2021.07.012>

946 Ghosh, P., Adkins, J., Affek, H., Balta, B., Guo, W., Schauble, E.A., Schrag, D., Eiler, J.M., 2006.  $^{13}\text{C}$ –  
947  $^{18}\text{O}$  bonds in carbonate minerals: A new kind of paleothermometer. *Geochimica et*  
948 *Cosmochimica Acta* 70, 1439–1456. <https://doi.org/10.1016/j.gca.2005.11.014>

949 Gonfiantini, R., Stichler, W., Rozanski, K., 1995. Standards and intercomparison materials distributed by  
950 the International Atomic Energy Agency for stable isotope measurements (No. IAEA-TECDOC--  
951 825).

952 Guo, W., Mosenfelder, J.L., Goddard, W.A., Eiler, J.M., 2009. Isotopic fractionations associated with  
953 phosphoric acid digestion of carbonate minerals: Insights from first-principles theoretical  
954 modeling and clumped isotope measurements. *Geochimica et Cosmochimica Acta* 73, 7203–  
955 7225. <https://doi.org/10.1016/j.gca.2009.05.071>

956 Guo, W., 2020. Kinetic clumped isotope fractionation in the DIC-H<sub>2</sub>O-CO<sub>2</sub> system: patterns, controls,  
957 and implications. *Geochimica et Cosmochimica Acta*, 268, pp.230-257.  
958 <https://doi.org/10.1016/j.gca.2019.07.055>

959 Hill, P.S., Schauble, E.A., Tripathi, A., 2014. Theoretical constraints on the effects of pH, salinity, and  
960 temperature on clumped isotope signatures of dissolved inorganic carbon species and  
961 precipitating carbonate minerals. *Geochimica et Cosmochimica Acta* 125, 610–652.  
962 <https://doi.org/10.1016/j.gca.2013.06.018>

963 Hill, P.S., Schauble, E.A. and Tripathi, A., 2020. Theoretical constraints on the effects of added  
964 cations on clumped, oxygen, and carbon isotope signatures of dissolved inorganic carbon species  
965 and minerals. *Geochimica et Cosmochimica Acta*, 269, pp.496-539.  
966 <https://doi.org/10.1016/j.gca.2019.10.016>

967 Johnson, K.S., 1982. Carbon dioxide hydration and dehydration kinetics in seawater1: CO<sub>2</sub> reaction  
968 kinetics. *Limnol. Oceanogr.* 27, 849–855. <https://doi.org/10.4319/lo.1982.27.5.0849>

969 Jones, J.P., Carricart-Ganivet, J.P., Prieto, R.I., Enríquez, S., Ackerson, M. and Gabitov, R.I., 2015.  
970 Microstructural variation in oxygen isotopes and elemental calcium ratios in the coral skeleton of  
971 *Orbicella annularis*. *Chemical Geology*, 419, pp.192-199.  
972 <https://doi.org/10.1016/j.chemgeo.2015.10.044>

973 Kernohan, J.C., 1964. The activity of bovine carbonic anhydrase in imidazole buffers. *Biochimica et*  
974 *Biophysica Acta (BBA) - Specialized Section on Enzymological Subjects* 81, 346–356.  
975 [https://doi.org/10.1016/0926-6569\(64\)90050-1](https://doi.org/10.1016/0926-6569(64)90050-1)

976 Kimball, J., Eagle, R., Dunbar, R., 2016. Carbonate “clumped” isotope signatures in aragonitic  
977 scleractinian and calcitic gorgonian deep-sea corals. *Biogeosciences* 13, 6487–6505.  
978 <https://doi.org/10.5194/bg-13-6487-2016>

979 Knoche, W., 1980. Chemical Reactions of CO<sub>2</sub> in Water, in: Bauer, C., Gros, G., Bartels, H. (Eds.),  
980 Biophysics and Physiology of Carbon Dioxide, *Proceedings in Life Sciences*. Springer Berlin  
981 Heidelberg, Berlin, Heidelberg, pp. 3–11. [https://doi.org/10.1007/978-3-642-67572-0\\_1](https://doi.org/10.1007/978-3-642-67572-0_1)

982 Lindskog, S., 1997. Structure and mechanism of carbonic anhydrase. *Pharmacology & Therapeutics* 74,  
983 1–20. [https://doi.org/10.1016/S0163-7258\(96\)00198-2](https://doi.org/10.1016/S0163-7258(96)00198-2)

984 Lucarelli, J., Carroll, H., Elliott, B., Eagle, R., Tripathi, A., 2021. Equilibrated gas and carbonate standard-  
985 derived paired clumped isotope ( $\Delta 47$  and  $\Delta 48$ ) values on the absolute reference frame (preprint).  
986 Physical Sciences and Mathematics. <https://doi.org/10.31223/X5T318>

987 McConnaughey, T., 1989. <sup>13</sup>C and <sup>18</sup>O isotopic disequilibrium in biological carbonates: II. In vitro  
988 simulation of kinetic isotope effects. *Geochimica et Cosmochimica Acta* 53, 163–171.  
989 [https://doi.org/10.1016/0016-7037\(89\)90283-4](https://doi.org/10.1016/0016-7037(89)90283-4)

990 Miller, R.F., Berkshire, D.C., Kelley, J.J. and Hood, D.W., 1971. Method for determination of reaction  
991 rates of carbon dioxide with water and hydroxyl ion in seawater. *Environmental Science &*  
992 *Technology*, 5(2), pp.127-133. <https://doi.org/10.1021/es60049a006>

- 993 Miyamoto, H., Miyashita, T., Okushima, M., Nakano, S., Morita, T., Matsushiro, A., 1996. A carbonic  
994 anhydrase from the nacreous layer in oyster pearls. *Proceedings of the National Academy of*  
995 *Sciences* 93, 9657–9660. <https://doi.org/10.1073/pnas.93.18.9657>
- 996 Moya, A., Tambutté, S., Bertucci, A., Tambutté, E., Lotto, S., Vullo, D., Supuran, C.T., Allemand, D.,  
997 Zoccola, D., 2008. Carbonic Anhydrase in the Scleractinian Coral *Stylophora pistillata*. *Journal*  
998 *of Biological Chemistry* 283, 25475–25484. <https://doi.org/10.1074/jbc.M804726200>
- 999 Nimer, N.A., Guan, Q., Merrett, M.J., 1994. Extra- and intra-cellular carbonic anhydrase in relation to  
1000 culture age in a high-calcifying strain of *Emiliana huxleyi* Lohmann. *New Phytologist* 126, 601–  
1001 607. <https://doi.org/10.1111/j.1469-8137.1994.tb02954.x>
- 1002 Passey, B.H., Henkes, G.A., 2012. Carbonate clumped isotope bond reordering and geospeedometry.  
1003 *Earth and Planetary Science Letters* 351–352, 223–236.  
1004 <https://doi.org/10.1016/j.epsl.2012.07.021>
- 1005 Rost, B., Riebesell, U., Burkhardt, S. and Sültemeyer, D., 2003. Carbon acquisition of bloom-forming  
1006 marine phytoplankton. *Limnology and oceanography*, 48(1), pp.55-67.  
1007 <https://doi.org/10.4319/lo.2003.48.1.0055>
- 1008 Saenger, C., Affek, H.P., Felis, T., Thiagarajan, N., Lough, J.M., Holcomb, M., 2012. Carbonate clumped  
1009 isotope variability in shallow water corals: Temperature dependence and growth-related vital  
1010 effects. *Geochimica et Cosmochimica Acta* 99, 224–242.  
1011 <https://doi.org/10.1016/j.gca.2012.09.035>
- 1012 Schauble, E.A., Ghosh, P., Eiler, J.M., 2006. Preferential formation of <sup>13</sup>C–<sup>18</sup>O bonds in carbonate  
1013 minerals, estimated using first-principles lattice dynamics. *Geochimica et Cosmochimica Acta* 70,  
1014 2510–2529. <https://doi.org/10.1016/j.gca.2006.02.011>
- 1015 Spooner, Peter T., Weifu Guo, Laura F. Robinson, Nivedita Thiagarajan, Katharine R. Hendry, Brad E.  
1016 Rosenheim, and Melanie J. Leng. "Clumped isotope composition of cold-water corals: A role for  
1017 vital effects?." *Geochimica et Cosmochimica Acta* 179 (2016): 123-141.  
1018 <https://doi.org/10.1016/j.gca.2016.01.023>
- 1019 Staudigel, P.T. and Swart, P.K., 2018. A kinetic difference between <sup>12</sup>C-and <sup>13</sup>C-bound oxygen  
1020 exchange rates results in decoupled  $\delta^{18}\text{O}$  and  $\Delta 47$  values of equilibrating DIC solutions.  
1021 *Geochemistry, Geophysics, Geosystems*, 19(8), pp.2371-2383.  
1022 <https://doi.org/10.1029/2018GC007500>
- 1023 Swart, Peter K., Chaojin Lu, Evan W. Moore, Megan E. Smith, Sean T. Murray, and Philip T. Staudigel.  
1024 "A calibration equation between  $\Delta 48$  values of carbonate and temperature." *Rapid*  
1025 *Communications in Mass Spectrometry* 35, no. 17 (2021): e9147.  
1026 <https://doi.org/10.1002/rcm.9147>
- 1027 Tang, J., Dietzel, M., Böhm, F., Köhler, S.J. and Eisenhauer, A., 2008. Sr<sup>2+</sup>/Ca<sup>2+</sup> and <sup>44</sup>Ca/<sup>40</sup>Ca  
1028 fractionation during inorganic calcite formation: II. Ca isotopes. *Geochimica et Cosmochimica*  
1029 *Acta*, 72(15), pp.3733-3745. <https://doi.org/10.1016/j.gca.2008.05.033>
- 1030 Tang, J., Dietzel, M., Fernandez, A., Tripathi, A.K., Rosenheim, B.E., 2014. Evaluation of kinetic effects  
1031 on clumped isotope fractionation ( $\Delta 47$ ) during inorganic calcite precipitation. *Geochimica et*  
1032 *Cosmochimica Acta* 134, 120–136. <https://doi.org/10.1016/j.gca.2014.03.005>
- 1033 Thiagarajan, N., Adkins, J., Eiler, J., 2011. Carbonate clumped isotope thermometry of deep-sea corals  
1034 and implications for vital effects. *Geochimica et Cosmochimica Acta* 75, 4416–4425.  
1035 <https://doi.org/10.1016/j.gca.2011.05.004>

1036 Tripathi, A.K., Hill, P.S., Eagle, R.A., Mosenfelder, J.L., Tang, J., Schauble, E.A., Eiler, J.M., Zeebe, R.E.,  
1037 Uchikawa, J., Coplen, T.B., Ries, J.B., Henry, D., 2015. Beyond temperature: Clumped isotope  
1038 signatures in dissolved inorganic carbon species and the influence of solution chemistry on  
1039 carbonate mineral composition. *Geochimica et Cosmochimica Acta* 166, 344–371.  
1040 <https://doi.org/10.1016/j.gca.2015.06.021>

1041 Trotter, J., Montagna, P., McCulloch, M., Silenzi, S., Reynaud, S., Mortimer, G., Martin, S., Ferrier-  
1042 Pagès, C., Gattuso, J.-P., Rodolfo-Metalpa, R., 2011. Quantifying the pH ‘vital effect’ in the  
1043 temperate zooxanthellate coral *Cladocora caespitosa*: Validation of the boron seawater pH proxy.  
1044 *Earth and Planetary Science Letters* 303, 163–173. <https://doi.org/10.1016/j.epsl.2011.01.030>

1045 Uchikawa, J., Zeebe, R.E., 2012. The effect of carbonic anhydrase on the kinetics and equilibrium of the  
1046 oxygen isotope exchange in the CO<sub>2</sub>–H<sub>2</sub>O system: Implications for  $\delta^{18}\text{O}$  vital effects in biogenic  
1047 carbonates. *Geochimica et Cosmochimica Acta* 95, 15–34.  
1048 <https://doi.org/10.1016/j.gca.2012.07.022>

1049 Uchikawa, J., Chen, S., Eiler, J.M., Adkins, J.F. and Zeebe, R.E., 2021. Trajectory and timescale of  
1050 oxygen and clumped isotope equilibration in the dissolved carbonate system under normal and  
1051 enzymatically-catalyzed conditions at 25° C. *Geochimica et Cosmochimica Acta*, 314, pp.313-  
1052 333. <https://doi.org/10.1016/j.gca.2021.08.014>

1053 Upadhyay, D., Lucarelli, J., Arnold, A., Flores, R., Bricker, H., Ulrich, R.N., Jesmok, G., Santi, L.,  
1054 Defliese, W., Eagle, R.A. and Carroll, H.M., 2021. Carbonate clumped isotope analysis ( $\Delta 47$ ) of  
1055 21 carbonate standards determined via gas-source isotope-ratio mass spectrometry on four  
1056 instrumental configurations using carbonate-based standardization and multiyear data sets. *Rapid*  
1057 *Communications in Mass Spectrometry*, 35(17), p.e9143. <https://doi.org/10.1002/rcm.9143>

1058 Usdowski, E., Michaelis, J., Boettcher, M., Hoefs, J., 1991. Factors for the oxygen isotope equilibrium  
1059 fractionation between aqueous and gaseous CO<sub>2</sub>, carbonic acid, bicarbonate, carbonate, and  
1060 water (19°C). *Zeitschrift fur physikalische chemie-international journal of research in physical*  
1061 *chemistry & Chemical Physics* 237–249.

1062 Wang, Z., Schauble, E.A., Eiler, J.M., 2004. Equilibrium thermodynamics of multiply substituted  
1063 isotopologues of molecular gases. *Geochimica et Cosmochimica Acta* 68, 4779–4797.  
1064 <https://doi.org/10.1016/j.gca.2004.05.039>

1065 Watkins, J.M., Hunt, J.D., Ryerson, F.J., DePaolo, D.J., 2014. The influence of temperature, pH, and  
1066 growth rate on the  $\delta^{18}\text{O}$  composition of inorganically precipitated calcite. *Earth and Planetary*  
1067 *Science Letters* 404, 332–343. <https://doi.org/10.1016/j.epsl.2014.07.036>

1068 Watkins, J.M. and Hunt, J.D., 2015. A process-based model for non-equilibrium clumped isotope effects  
1069 in carbonates. *Earth and Planetary Science Letters*, 432, pp.152-165.  
1070 <https://doi.org/10.1016/j.epsl.2015.09.042>

1071 Weise, A. and Kluge, T., 2020. Isotope exchange rates in dissolved inorganic carbon between 40° C and  
1072 90° C. *Geochimica et Cosmochimica Acta*, 268, pp.56-72.  
1073 <https://doi.org/10.1016/j.gca.2019.09.032>

1074 Winograd, I.J., Coplen, T.B., Landwehr, J.M., Riggs, A.C., Ludwig, K.R., Szabo, B.J., Kolesar, P.T.,  
1075 Revesz, K.M., 1992. Continuous 500,000-Year Climate Record from Vein Calcite in Devils Hole,  
1076 Nevada. *Science* 258, 255–260. <https://doi.org/10.1126/science.258.5080.255>

1077 Winograd, I.J., Coplen, T.B., Szabo, B.J., Riggs, A.C., 1988. A 250,000-Year Climatic Record from  
1078 Great Basin Vein Calcite: Implications for Milankovitch Theory. *Science* 242, 1275–1280.  
1079 <https://doi.org/10.1126/science.242.4883.1275>

1080 Wolthers, M., Nehrke, G., Gustafsson, J.P. and Van Cappellen, P., 2012. Calcite growth kinetics:  
1081 Modeling the effect of solution stoichiometry. *Geochimica et Cosmochimica Acta*, 77, pp.121-  
1082 134. <https://doi.org/10.1016/j.gca.2011.11.003>

1083 Yu, Z., Xie, L., Lee, S., Zhang, R., 2006. A novel carbonic anhydrase from the mantle of the pearl oyster  
1084 (*Pinctada fucata*). *Comparative Biochemistry and Physiology Part B: Biochemistry and*  
1085 *Molecular Biology* 143, 190–194. <https://doi.org/10.1016/j.cbpb.2005.11.006>

1086 Zeebe, R.E., Wolf-Gladrow, D.A., 2001. CO<sub>2</sub> in seawater: equilibrium, kinetics, isotopes, *Elsevier*  
1087 *oceanography series*. Elsevier, Amsterdam; New York.

1088 Zeebe, R.E., 2020. Oxygen isotope fractionation between water and the aqueous hydroxide ion.  
1089 *Geochimica et Cosmochimica Acta*, 289, pp.182-195. <https://doi.org/10.1016/j.gca.2020.08.025>

1090 Zeebe, R.E., 2014. Kinetic fractionation of carbon and oxygen isotopes during hydration of carbon  
1091 dioxide. *Geochimica et Cosmochimica Acta*, 139, pp.540-552.  
1092 <https://doi.org/10.1016/j.gca.2014.05.005>

1093

1094

1095

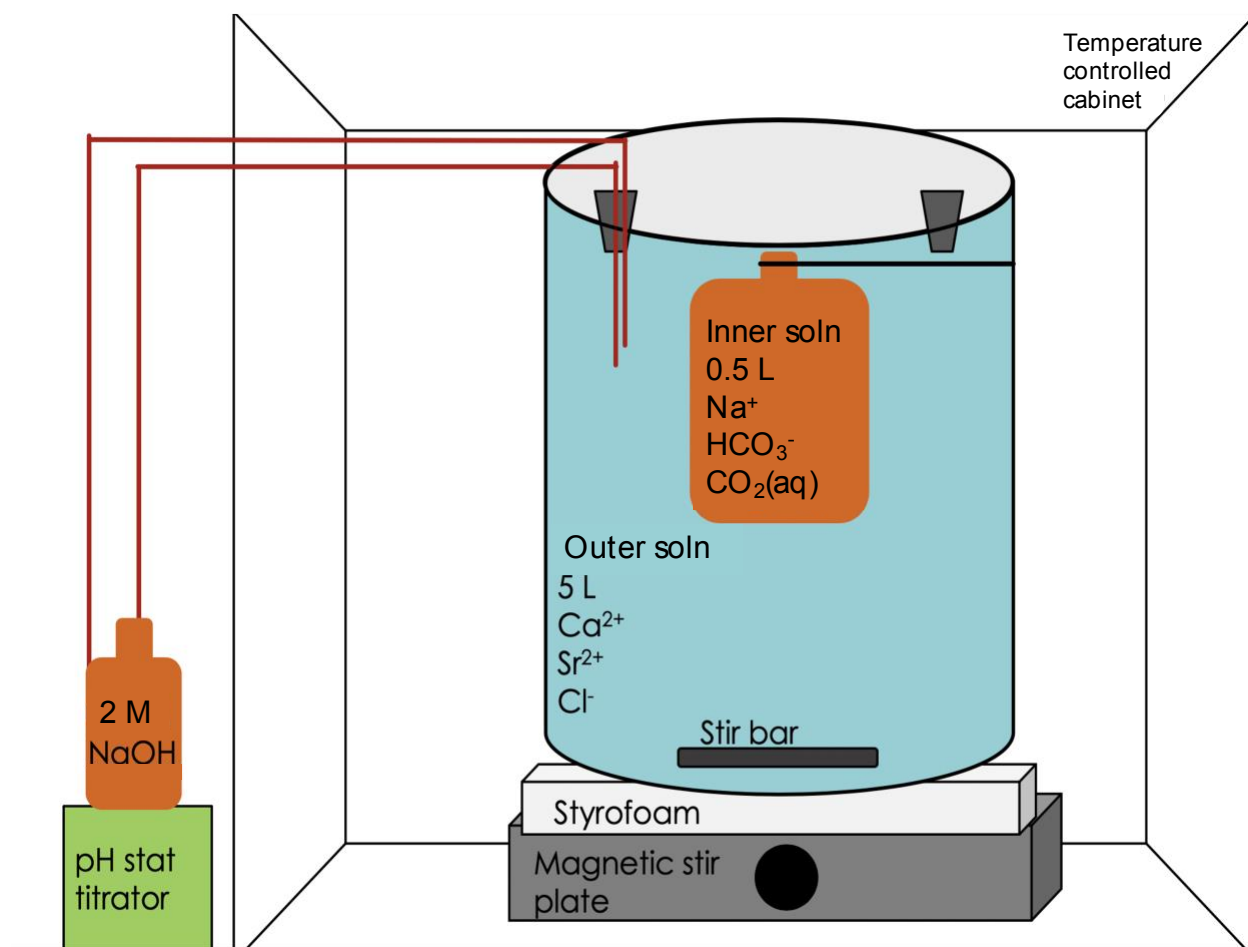


**Figure 1.** Schematic of the precipitation apparatus used for this work. The inner bottle is a 0.5 L, 2 mm thick polyethylene bottle that serves as a membrane through which CO<sub>2</sub> diffuses into the outer solution. The outer solution is inside a 5 L container that contains Ca<sup>2+</sup> from CaCl. A pH-stat titrator holds the pH of the outer solution constant by titrating NaOH. The temperature is held constant by placing the entire apparatus inside a temperature-controlled cabinet. Adapted from Dietzel and Usdowski (1996), Dietzel et al. (2004), Tang et al., (2008), and Tang et al. (2014).

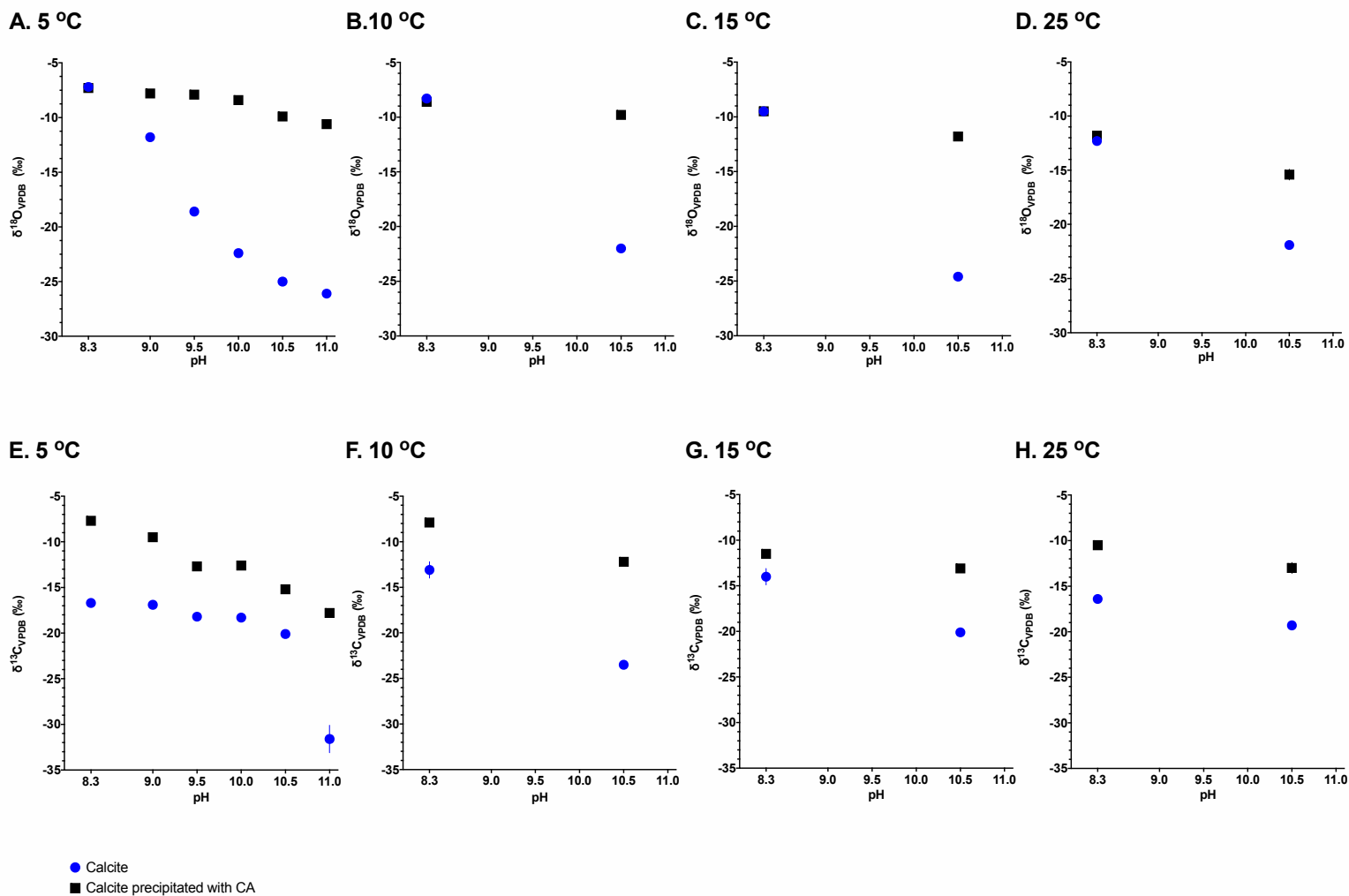


**Figure 2.**  $\delta^{18}\text{O}$  and  $\delta^{13}\text{C}$  with precipitation pH for calcite precipitated with and without carbonic anhydrase (CA) at variable temperature.  $\delta^{18}\text{O}$  versus precipitation pH for A) 5 °C, B) 10 °C, C) 15 °C, and D) 25 °C.  $\delta^{13}\text{C}$  versus precipitation pH for E) 5 °C, F) 10 °C, G) 15 °C, and H) 25 °C.

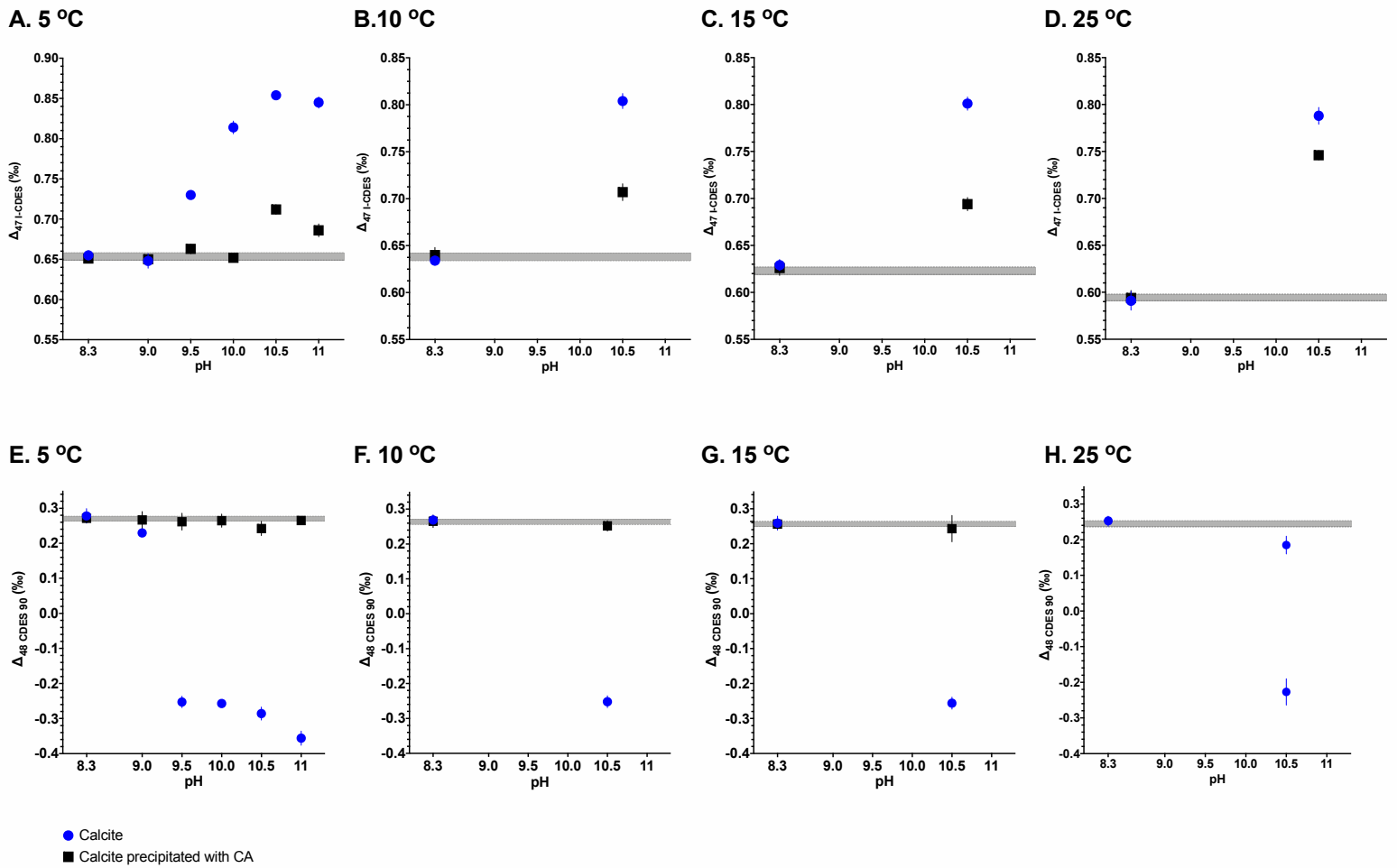


**Figure 3.**  $\Delta_{47}$  relative to pH at variable temperature for calcite precipitated with and without carbonic anhydrase (CA). A) 5 °C, B) 10 °C, C) 15 °C, and D) 25 °C, and  $\Delta_{48}$  relative to pH at E) 5 °C, F) 10 °C, G) 15 °C, and H) 25 °C. Enrichments in  $\Delta_{47}$  and depletions in  $\Delta_{48}$  in samples precipitated at pH > 9.5. The gray bar is the range of expected equilibrium values derived from Swart et al. (2021), Fiebig et al. (2021), Lucarelli et al. (2021), and this study.

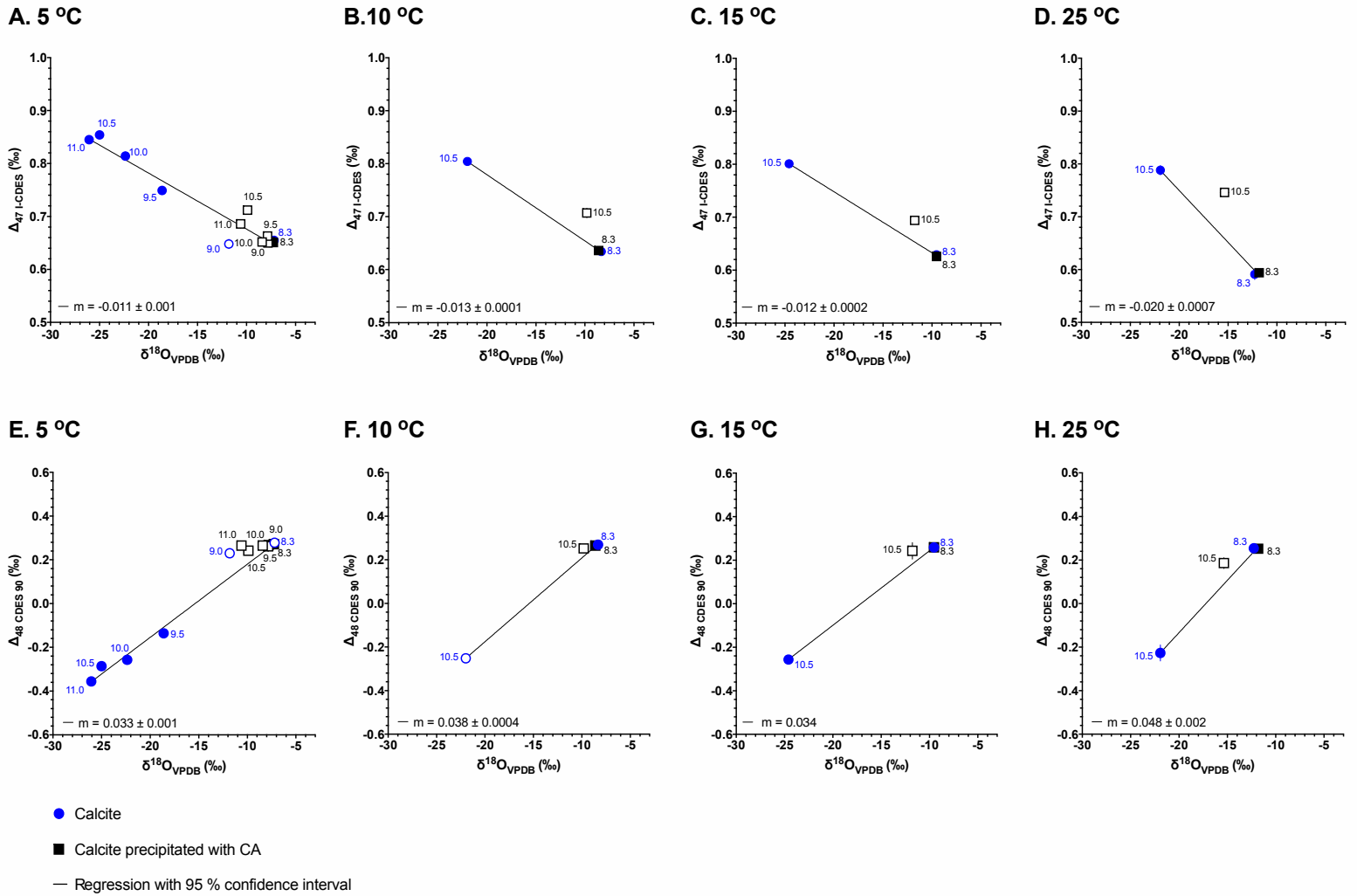


**Figure 4.**  $\Delta_{47}$  and  $\delta^{18}\text{O}$  at variable temperature for calcite precipitated with and without carbonic anhydrase (CA). A) 5 °C ( $r^2 = 0.96$ ), B) 10 °C ( $r^2 = 0.99$ ), C) 15 °C ( $r^2 = 0.99$ ), and D) 25 °C ( $r^2 = 0.99$ ), and  $\Delta_{48}$  and  $\delta^{18}\text{O}$  at E) 5 °C ( $r^2 = 0.99$ ), F) 10 °C ( $r^2 = 0.99$ ), G) 15 °C ( $r^2 = 0.99$ ), and H) 25 °C ( $r^2 = 0.99$ ). Numbers next to each data point indicate precipitation pH. Samples at elevated pH are depleted in  $\delta^{18}\text{O}$  and  $\Delta_{47}$ , and enriched in  $\Delta_{48}$  relative to expected equilibrium values. Regressions are between quasi-equilibrium samples synthesized at pH 8.3 and samples synthesized at elevated pHs without CA, with negative slopes for  $\Delta_{47}$  relative to  $\delta^{18}\text{O}$ , and positive slopes for  $\Delta_{48}$  relative to  $\delta^{18}\text{O}$ . Data with open symbols are not included in regression.

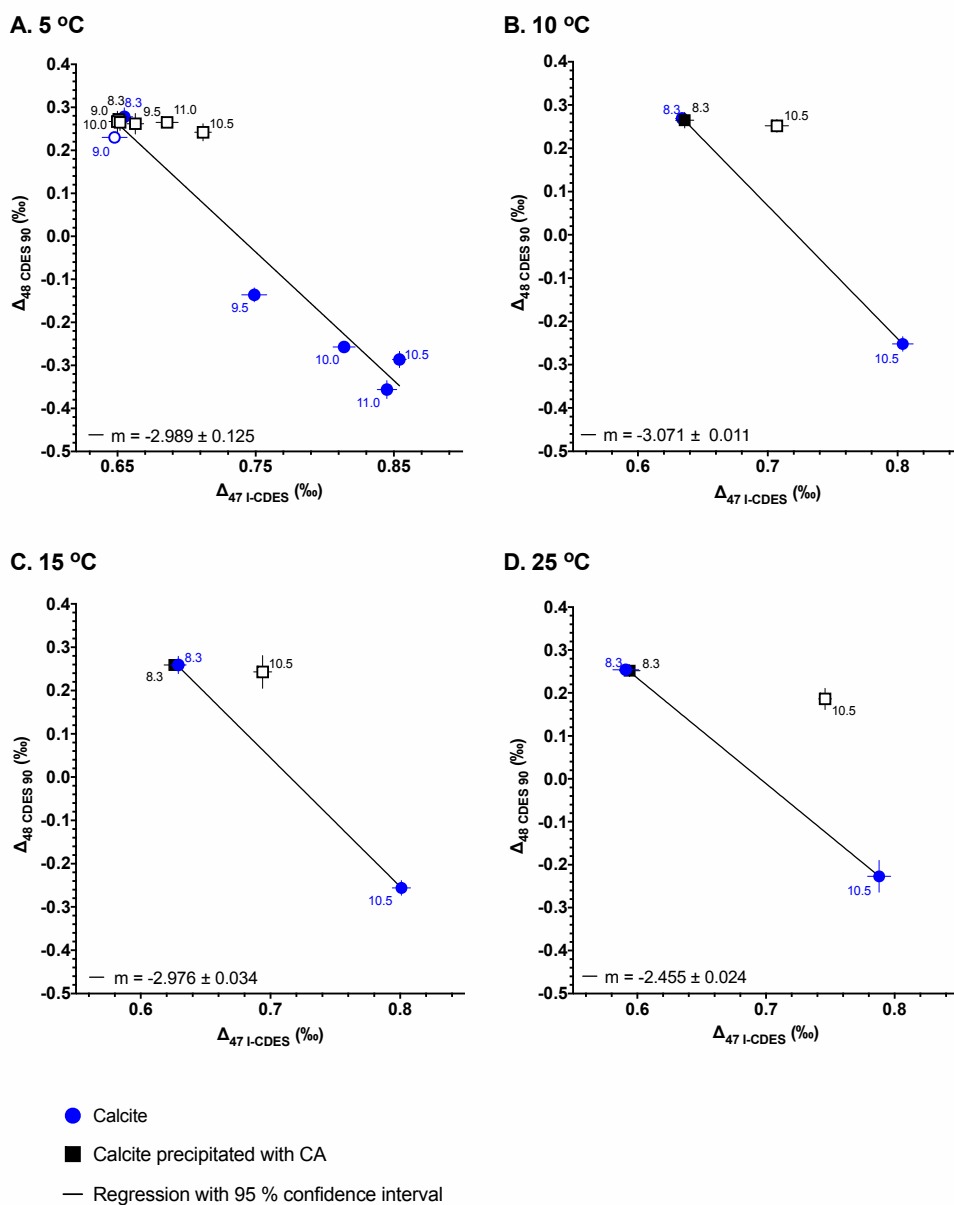


**Figure 5.**  $\Delta_{47}$  and  $\Delta_{48}$  for calcite synthesized at variable pH with and without CA at different temperatures. A) 5 °C ( $r^2 = 0.95$ ), B) 10 °C ( $r^2 = 0.99$ ), C) 15 °C ( $r^2 = 0.99$ ), and D) 25 °C ( $r^2 = 0.99$ ). Numbers next to each data point indicate precipitation pH. Regressions are between quasi-equilibrium samples synthesized at pH 8.3 and samples synthesized at elevated pHs without CA, with negative slopes observed for all experiments. Data with open symbols are not included in the regressions.

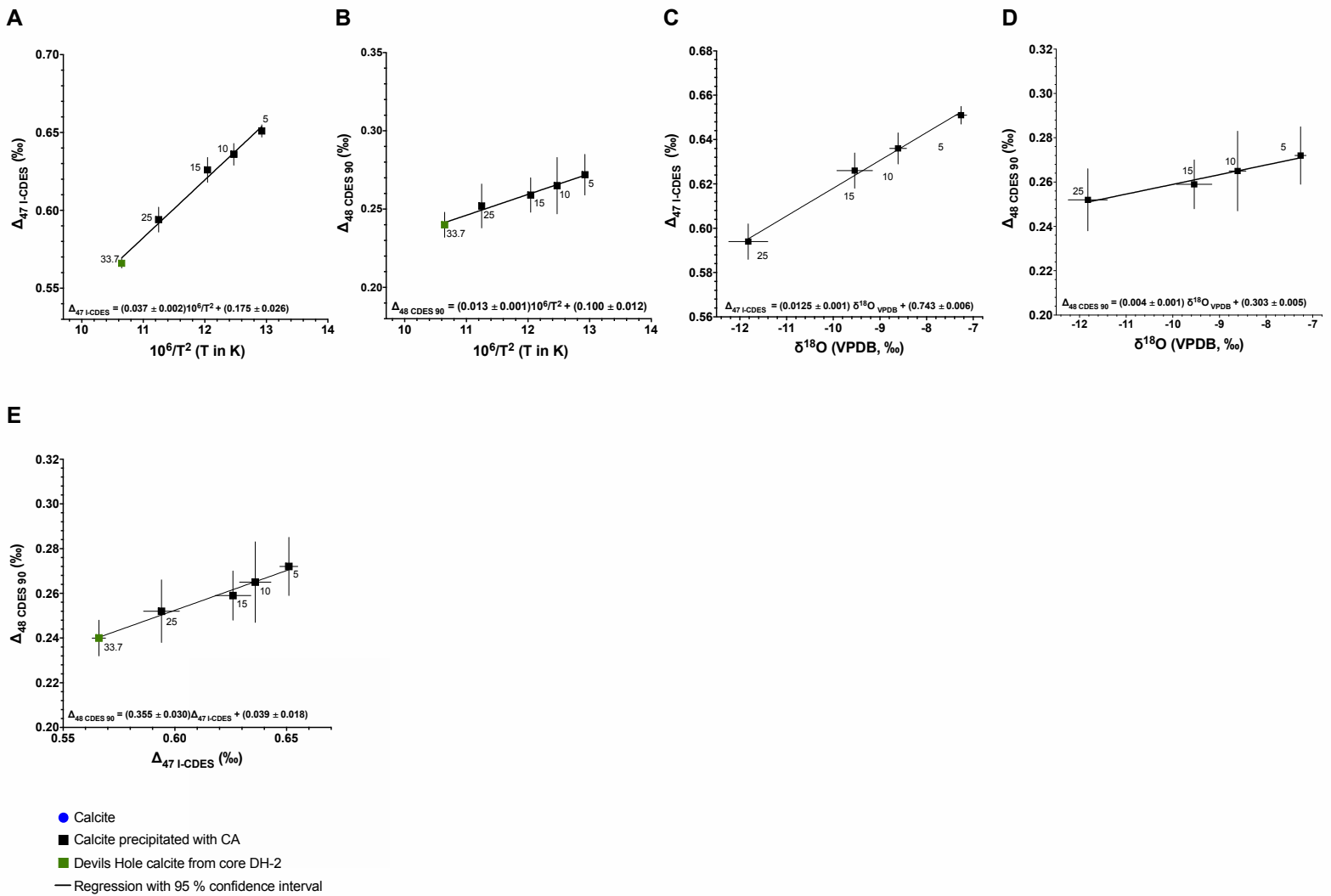


**Figure 6.** Quasi-equilibrium regressions for clumped isotope data and precipitation temperature, A)  $\Delta_{47}$  and  $10^6T^{-2}$  ( $r^2 = 0.99$ ) and B)  $\Delta_{48}$  and  $10^6T^{-2}$  ( $r^2 = 0.98$ ) with temperature in Kelvin. Quasi-equilibrium regressions for C)  $\Delta_{47}$  and  $\delta^{18}\text{O}$  ( $r^2 = 0.99$ ) and D)  $\Delta_{48}$  and  $\delta^{18}\text{O}$  ( $r^2 = 0.97$ ). Quasi-equilibrium regression for  $\Delta_{47}$  and  $\Delta_{48}$  ( $r^2 = 0.98$ ). Data on all panels is for samples precipitated at pH 8.3 with CA and for Devils Hole calcite (DH-2), which is thought to have formed in near isotopic equilibrium at a temperature of 33.7 °C (Winograd et al., 1988; Winograd et al., 1992; Coplen, 2007; Kluge et al., 2014; Tripathi et al., 2015; Daëron et al., 2019; Bajani et al., 2021).

A. 5 °C

B. 25 °C

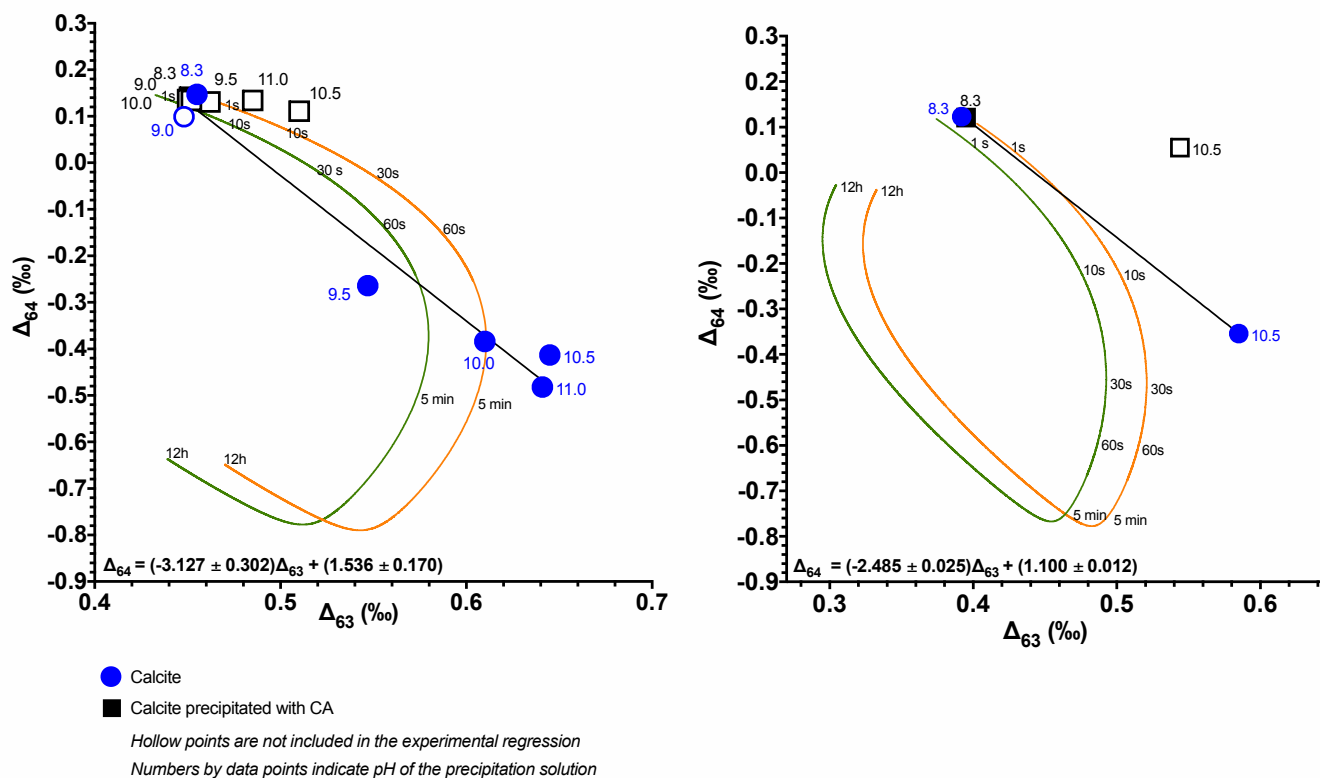


**Figure 7.** Experimental results compared to IsoDIC model predictions for the evolution of  $\text{HCO}_3^-$  and  $\text{CO}_3^{2-}$  isotopic composition at different temperatures and as a function of time. Experimental data are for calcite precipitated with (blue circles) and without CA (black squares) at varying pH. Numbers by data points indicate pH of precipitation solution. Regression through data (black line) and 95% confidence interval also shown. Calculations are for end member compositions at A) 5 °C and pH 10.5 and B) 25 °C and pH 10.5. Green trajectory shows modelled values for  $\text{CO}_3^{2-}$  and orange trajectory shows modelled values for  $\text{HCO}_3^-$ . Numbers on model trajectories indicate evolution time after the start of calcite precipitation. IsoDIC model software we used for our calculations was from Guo (2020).

Default model

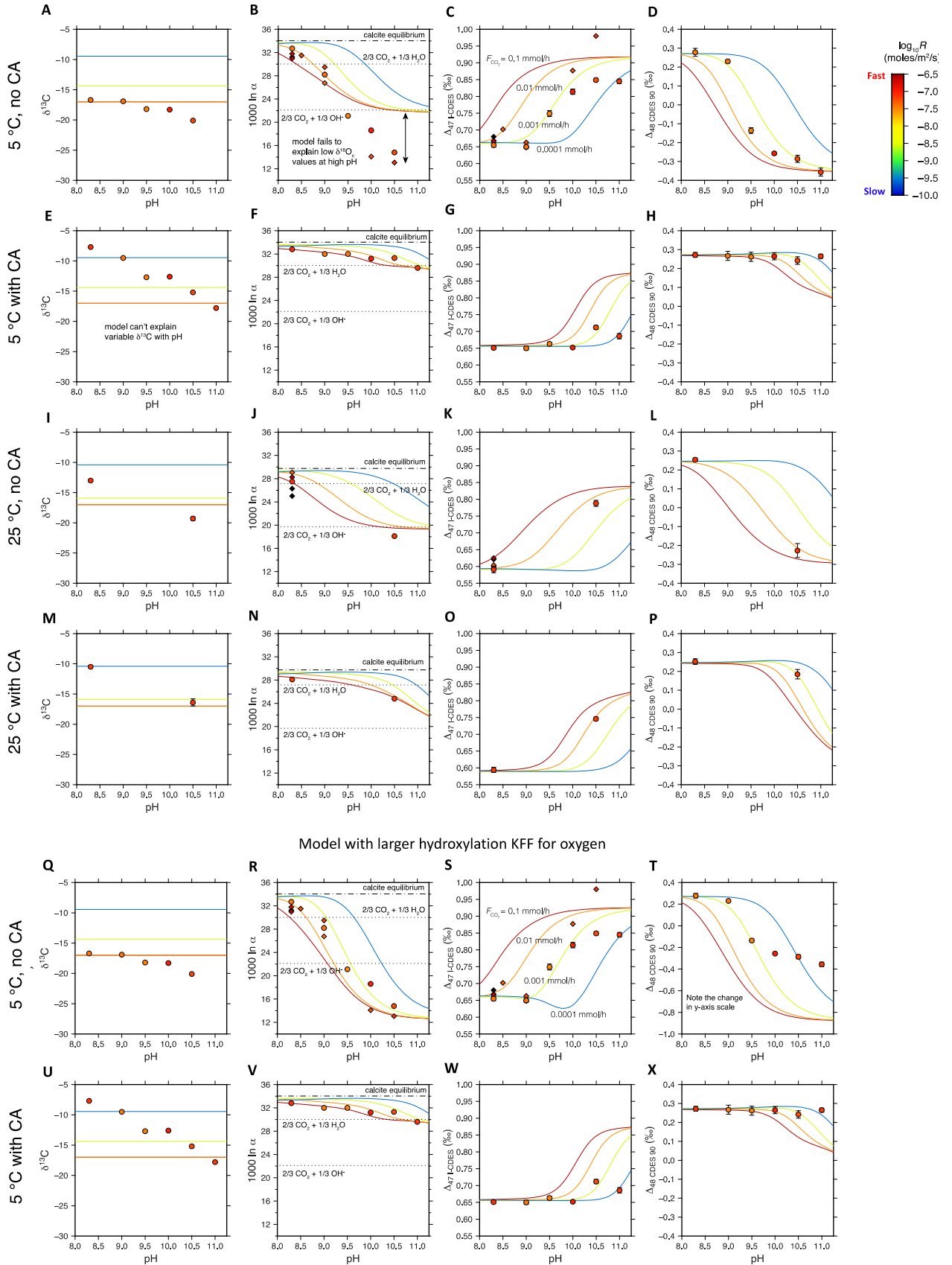


**Figure 8.** Experimental results from this work compared to data from Tang et al. (2014) and box model predictions. Symbol color indicates precipitation rate with color scale shown. Black points have precipitation faster than a  $\log R$  (mol/m<sup>2</sup>/s) value of -6.5. Colored curves show  $\alpha_{\text{carb-water}}$ ,  $\Delta_{47}$ , and  $\Delta_{48}$  of calcite predicted by box model for different precipitation rates, with kinetic limit reflecting CO<sub>2</sub> hydration and hydroxylation and presence or absence of carbonic anhydrase (CA; calculations utilize values of 0 or 0.25  $\mu\text{M}$  CA). Panels A-P show default model conditions with and with and without CA, and panels Q-X show the model with larger KFFs for oxygen. Clumped isotopic compositions of calcite are predicted to be sensitive to temperature, growth rate, and pH (Watkins and Hunt, 2015; Tripathi et al., 2015; Guo, 2020; Uchikawa et al., 2021).

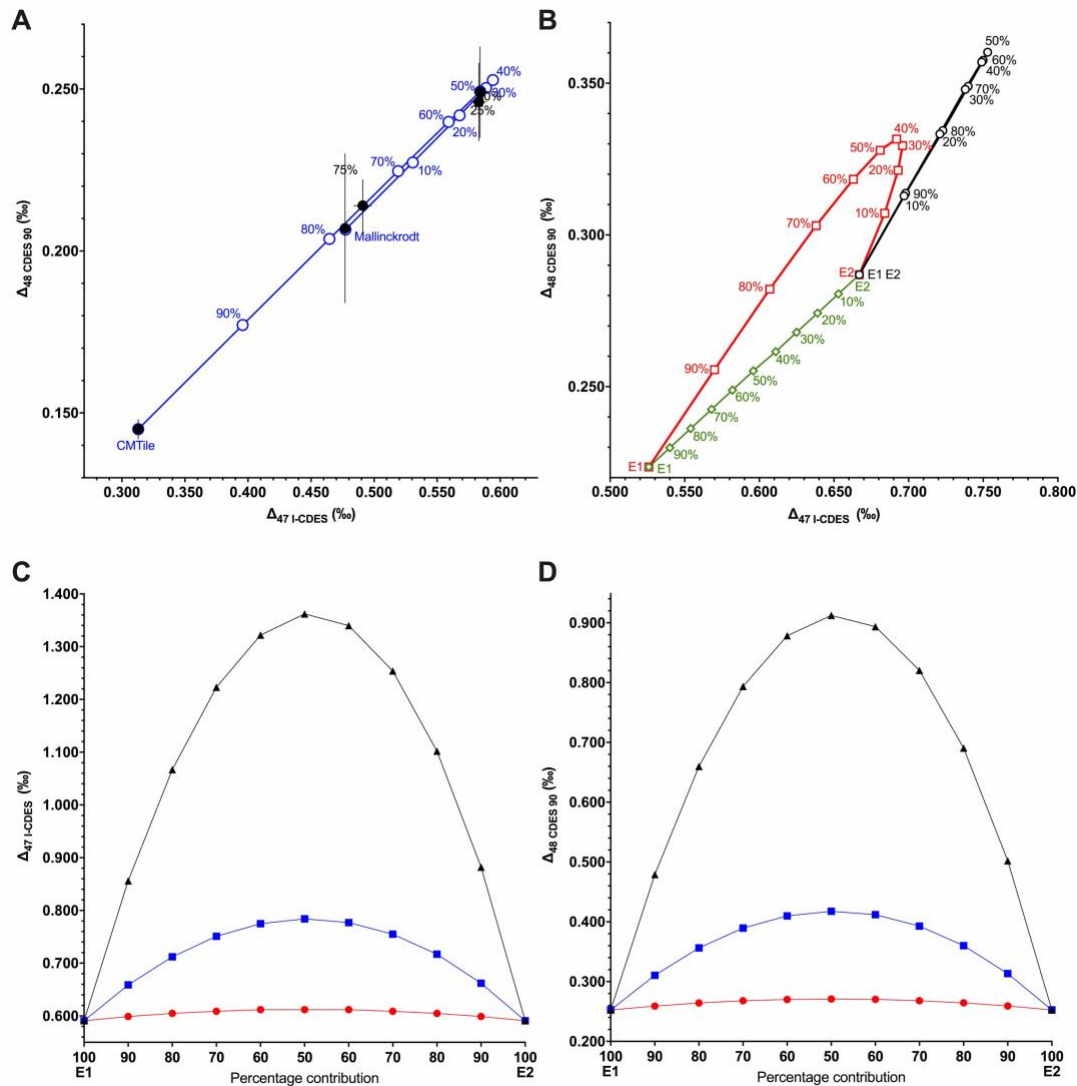


**Figure 9.** Predicted and observed clumped isotope composition for mixing experiments. A)  $\Delta_{47}$  and  $\Delta_{48}$  for non-linear mixing model predictions compared to experimental results. Two internal standards, CM Tile and Mallinckrodt, were used as endmembers. B) Mixing model predictions with different endmembers. Red line is for end members with a 0.141‰ and 0.063 ‰ difference in  $\Delta_{47}$  and  $\Delta_{48}$ , and a 20 ‰ difference in  $\delta^{18}\text{O}$  and  $\delta^{13}\text{C}$ . Green line endmembers with a 0.141‰ and 0.063 ‰ difference in  $\Delta_{47}$  and  $\Delta_{48}$ , and identical  $\delta^{18}\text{O}$  and  $\delta^{13}\text{C}$ . The difference in the clumped isotope values of the endmembers in the green and red lines is approximately equivalent to a 50 °C temperature difference. Black line endmembers with identical clumped isotope values and a 20 ‰ difference in  $\delta^{18}\text{O}$  and  $\delta^{13}\text{C}$ . C)  $\Delta_{47}$  and percentage contribution of each endmember for mixing model predictions where the endmembers have identical  $\Delta_{47}$  values and a 60 ‰ difference in  $\delta^{18}\text{O}$  and  $\delta^{13}\text{C}$  (black line), 30 ‰ difference in  $\delta^{18}\text{O}$  and  $\delta^{13}\text{C}$  (blue line), and 10 ‰ difference in  $\delta^{18}\text{O}$  and  $\delta^{13}\text{C}$  (red line). D)  $\Delta_{48}$  and percentage contribution of each endmember for mixing model predictions where the endmembers have identical  $\Delta_{48}$  values and a 60 ‰ difference in  $\delta^{18}\text{O}$  and  $\delta^{13}\text{C}$  (black line), 30 ‰ difference in  $\delta^{18}\text{O}$  and  $\delta^{13}\text{C}$  (blue line), and 10 ‰ difference in  $\delta^{18}\text{O}$  and  $\delta^{13}\text{C}$  (red line).

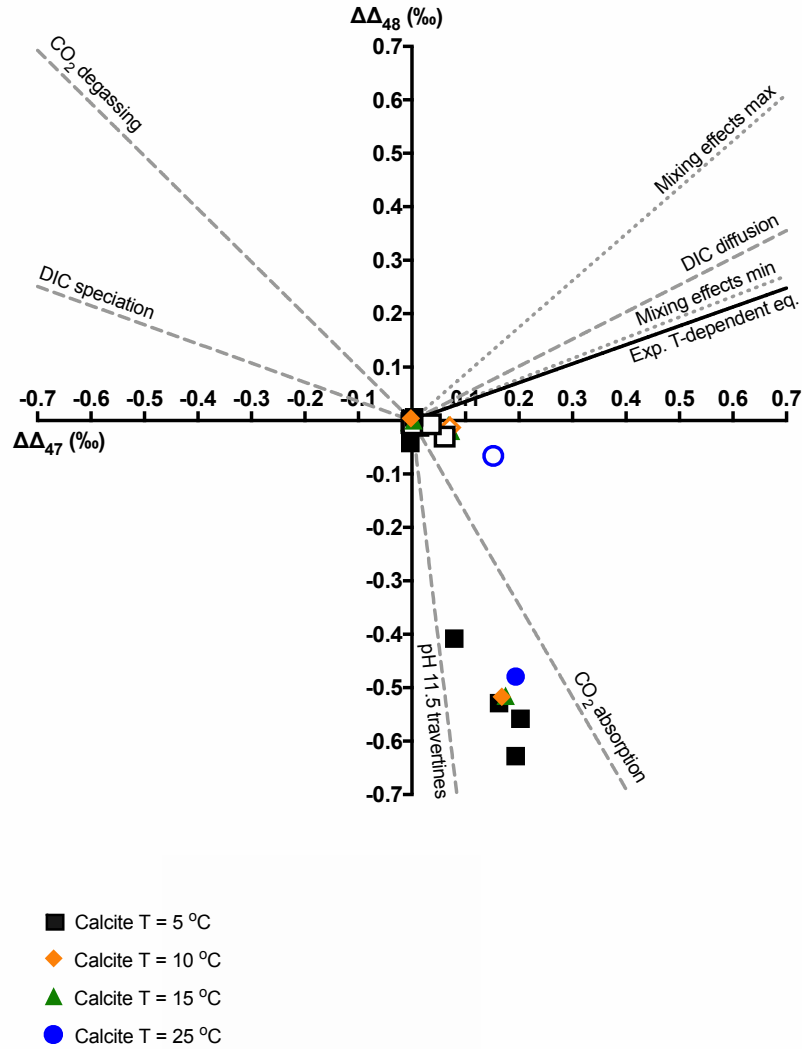


**Figure 10.**  $\Delta\Delta_{47}$  and  $\Delta\Delta_{48}$  data from experiments compared to theoretical predictions. Colored symbols are for calcite from this study synthesized at different temperatures. Open symbols are for samples grown with carbonic anhydrase (CA). Kinetic slopes include  $\Delta_{63}$  and  $\Delta_{64}$  values for  $\text{HCO}_3^-$  endmembers produced through varying processes (Guo, 2020) that we use to predict  $\Delta_{47}$  and  $\Delta_{48}$ , and mixing model predictions for calcite (this study). Experimental  $T$ -dependent equilibrium slope = 0.387. Slopes published in Guo (2020) using IsoDIC modeling software and our mixing model predicted non-equilibrium slopes for different processes. DIC speciation = -0.358; DIC diffusion = 0.506,  $\text{CO}_2$  degassing at pH 8 = -0.990;  $\text{CO}_2$  absorption at pH 9 = -1.72; travertine precipitation at pH 11.5 = -8.33; mixing values = 0.387 to 0.872.

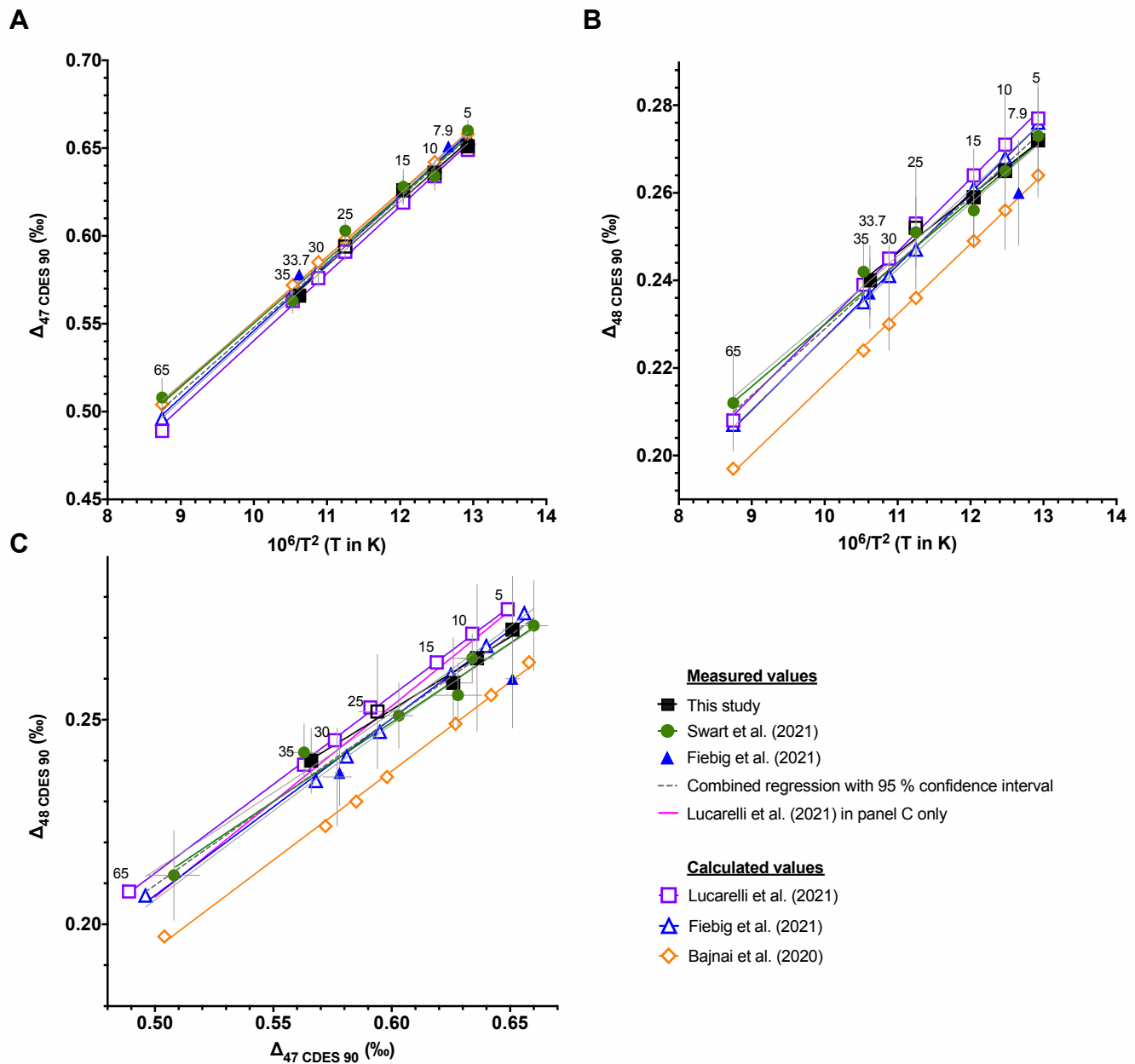


**Figure 11.** Comparison of  $\Delta_{47}$  and  $\Delta_{48}$  regressions from this work to published results. A)  $\Delta_{47}$  and  $10^6 T^{-2}$  with T in K, B)  $\Delta_{48}$  and  $10^6 T^{-2}$  with T in K, and C)  $\Delta_{47}$  and  $\Delta_{48}$ . Results for samples grown at pH 8.3 with carbonic anhydrase (CA) from this work are compared to experimentally-based regressions (Swart et al., 2021; Fiebig et al., 2021; Bajnai et al., 2020; Lucarelli et al., 2021). Bajnai et al. (2020) and Lucarelli et al. (2021) are based on theory from Hill et al. (2014) and Tripathi et al. (2015) with experimental AFFs. All regressions were determined to be statistically indistinguishable, and a combined regression was determined for the experimentally based regressions. Numbers by symbols indicate precipitation temperature in Celsius.

Table 1. Experimental conditions for precipitation experiments with and without carbonic anhydrase (CA). Mineralogy as determined by XRD indicated.

Temperature of precipitation (°C)	pH of precipitation solution	CA (yes or no)	Time from beginning of experiment until start of precipitation (days)	Total experiment time (days)	Precipitation rate ( $\log_{10}R$ with R in $\text{mol s}^{-1} \text{m}^{-2}$ )	Initial water $\delta^{18}\text{O}_{\text{VSMOW}}$ (‰)	Final water $\delta^{18}\text{O}_{\text{VSMOW}}$ (‰)	Calcite (weight %)	Vaterite (weight %)	Aragonite (weight %)
5	8.3	Y	23	34	-7.11	n/a	-9.52	100		
5	8.3	N	29	52	-7.43	n/a	-9.44	100		
5	9.0	Y	3	27	-7.45	-9.22	-9.14	100		
5	9.0	N	5	27	-7.41	-9.40	-9.31	100		
5	9.5	Y	1	26	-7.47	-9.37	-9.26	100		
5	9.5	N	<1	26	-7.48	-9.44	-9.33	100		
5	10.0	Y	<1	9	-7.02	-9.47	-9.13	100		
5	10.0	N	<1	9	-7.02	-9.64	-9.56	100		
5	10.5	Y	<1	14	-7.21	n/a	-9.07	100		
5	10.5	N	<1	14	-7.21	-9.37	-9.25	100		
5	11.0	Y	<1	12	-7.15	n/a	-9.44	100		
5	11.0	N	<1	12	-7.15	n/a	n/a	100		
10	8.3	Y	14	26	-7.15	-9.26	-9.40	100		
10	8.3	N	10	26	-7.27	-9.18	-9.35	100		
10	10.5	Y	1	15	-7.21	-8.83	-8.86	21	75	4
10	10.5	N	1	15	-7.21	-8.96	-9.01	100		
15	8.3	Y	9	20	-7.11	-9.03	-9.15	100		
15	8.3	N	9	20	-7.11	-9.16	-9.10	100		
15	10.5	Y	<1	14	-7.21	-9.22	-9.02	54	43	3
15	10.5	N	<1	14	-7.21	-9.34	-9.06	100		
25	8.3	Y	2	14	-7.15	-9.30	-9.29	100		
25	8.3	N	3	14	-7.11	-9.32	-9.33	100		
25	10.5	Y	<1	12	-7.15	-9.53	-9.38	72	2	26
25	10.5	N	<1	12	-7.15	-9.33	-9.29	60		40

Table 2. Mass spectrometer configurations used in this study.

Mass Spectrometer	Acid digestion T (°C)	Acid digestion method	Sample size (mg)	GC column with He carrier gas	Adsorption trap	m/z 44 ion beam intensity	Integration time (s)
Thermo Fisher MAT 253	90	common acid bath	5	x		16 V	720
Nu Instruments Perspective-1a	90	common acid bath	0.5	x		80-30 nA	1600
Nu Instruments Perspective -1b	70	individual vials	0.5		x	80-30 nA	1600
Nu Instruments Perspective-1c	90	common acid bath	0.5		x	80-30 nA	1600
Nu Instruments Perspective-2a	70	individual vials	0.5		x	80-30 nA	1200
Nu Instruments Perspective-2b	90	common acid bath	0.5		x	80-30 nA	1200

**Table 3.** Clumped and stable isotope data for all samples measured in this study. Calcite mineral  $\Delta_{63}$  and  $\Delta_{64}$  was calculated using equations from Lucarelli et al. (2021), which were based on theory from Hill et al. (2014) and Tripathi et al. (2015) and experimentally determined acid digestions fractionation factors (AFFs).

Temp. (°C)	pH	CA (yes or no)	$\Delta_{47+CDDES}$ (‰)	SE	N	$\Delta_{48 CDDES90}$ (‰)	SE	N	$\Delta_{63}$ (‰)	$\Delta_{64}$ (‰)	$\delta^{18}O_{VPDB}$ (‰)	SD	1000ln( $\alpha_{CaCO3-H2O}$ )	$\delta^{13}C_{VPDB}$ (‰)	SD
5	8.3	Y	0.651	0.004	15	0.272	0.013	10	0.451	0.141	-7.3	0.1	32.8	-7.7	0.0
5	8.3	N	0.655	0.006	5	0.278	0.021	4	0.455	0.147	-7.2	0.1	32.7	-16.7	0.1
5	9.0	Y	0.650	0.006	13	0.267	0.024	5	0.450	0.136	-7.8	0.1	32.0	-9.5	0.1
5	9.0	N	0.648	0.009	10	0.230	0.009	7	0.448	0.099	-11.8	0.1	28.2	-16.9	0.1
5	9.5	Y	0.663	0.005	12	0.262	0.024	7	0.462	0.131	-7.9	0.1	32.0	-12.7	0.1
5	9.5	N	0.749	0.009	6	-0.136	0.015	4	0.547	-0.264	-18.6	0.1	21.1	-18.2	0.1
5	10.0	Y	0.652	0.003	7	0.265	0.019	4	0.452	0.134	-8.4	0.1	31.2	-12.6	0.0
5	10.0	N	0.814	0.008	10	-0.257	0.007	4	0.610	-0.384	-22.4	0.2	18.6	-18.3	0.0
5	10.5	Y	0.712	0.006	7	0.242	0.020	5	0.510	0.111	-9.9	0.2	30.3	-15.2	0.1
5	10.5	N	0.849	0.005	8	-0.286	0.019	7	0.645	-0.413	-25.0	0.1	14.8	-20.1	0.0
5	11.0	Y	0.686	0.008	9	0.265	0.011	5	0.485	0.134	-10.6	0.1	29.6	-17.8	0.0
5	11.0	N	0.845	0.007	4	-0.356	0.021	4	0.641	-0.482	-26.1	0.1	n/a	-31.6	1.5
10	8.3	Y	0.636	0.007	8	0.265	0.018	8	0.436	0.134	-8.6	0.2	31.4	-7.9	0.2
10	8.3	N	0.634	0.005	9	0.269	0.014	8	0.434	0.138	-8.3	0.4	31.4	-13.1	0.9
10	10.5	Y	0.707	0.009	9	0.252	0.015	4	0.506	0.121	-9.8	0.0	29.7	-12.2	0.3
10	10.5	N	0.804	0.008	11	-0.252	0.017	4	0.601	-0.379	-22.0	0.2	17.3	-23.5	0.1
15	8.3	Y	0.626	0.008	12	0.259	0.011	7	0.426	0.128	-9.5	0.4	30.3	-11.5	0.1
15	8.3	N	0.629	0.006	10	0.259	0.020	6	0.429	0.128	-9.5	0.3	29.9	-14.0	0.9
15	10.5	Y	0.694	0.007	10	0.243	0.038	2	0.493	0.112	-11.8	0.4	28.1	-13.1	0.3
15	10.5	N	0.801	0.007	13	-0.256	0.017	5	0.598	-0.383	-24.6	0.3	14.9	-20.1	0.1
25	8.3	Y	0.594	0.008	17	0.252	0.015	9	0.395	0.121	-11.8	0.4	28.1	-10.5	0.2
25	8.3	N	0.591	0.010	12	0.254	0.009	7	0.392	0.123	-12.3	0.4	27.5	-16.4	0.2
25	10.5	Y	0.746	0.005	7	0.185	0.025	5	0.544	0.055	-15.4	0.5	24.8	-13.0	0.6
25	10.5	N	0.788	0.009	11	-0.227	0.037	4	0.585	-0.354	-21.9	0.2	18.1	-19.3	0.3

**Table 4.** Equilibrium and kinetic trajectories for clumped and bulk isotopes for calcite precipitated with varying temperature and pH with and without CA. Near equilibrium slopes were determined by precipitating calcite at pH 8.3 with CA at 5 °C, 10 °C, 15 °C, and 25 °C. Kinetic slopes at 5 °C were determined with a regression through samples precipitated at pH 8.3 with and without CA, and 9.5, 10.0, 10.5, and 11.0 without CA. Kinetic slopes at 10 °C, 15 °C, and 25 °C were determined by regressions through samples precipitated at pH 8.3 with and without CA, and at pH 10.5 without CA. Calcite mineral  $\Delta_{63}$  and  $\Delta_{64}$  were calculated using equations from Lucarelli et al. (2021), which use theory from Hill et al. (2014) and Tripati et al. (2015) with experimentally-determined compositionally-dependant acid digestion fractionation factors.

Temp. (°C)	Quasi-equilibrium or kinetic	Slope: $\Delta_{47\text{-}1\text{-}CDES}$ versus $\delta^{18}\text{O}_{VPDB}$	SE	Slope: $\Delta_{48\text{-}CDES90}$ versus $\delta^{18}\text{O}_{VPDB}$	SE	Slope: $\Delta_{47\text{-}1\text{-}CDES}$ versus $\Delta_{48\text{-}CDES90}$	SE	Slope: $\Delta_{64}$ versus $\Delta_{63}$
5 to 25	quasi-equilibrium	0.013	0.001	0.004	0.001	0.355	0.030	0.373
5	kinetic	-0.011	0.001	-0.033	0.001	-2.989	0.125	-3.127
10	kinetic	-0.013	0.000	-0.038	0.000	-3.071	0.011	-3.102
15	kinetic	-0.012	0.000	-0.034	n/a	-2.976	0.034	-2.996
25	kinetic	-0.020	0.001	-0.048	0.002	-2.455	0.024	-2.485

**Table 5.** Measured and model predicted clumped and bulk isotope values from a mixing experiment using two endmembers with varying clumped and bulk isotope compositions. Mix 1 is 75% Mallinckrodt and 25 % CM Tile. Mix 2 is 50 % Mallinckrodt and 50 % CM Tile. Mix 3 is 25 % Mallinckrodt and 75 % CM Tile.

Sample	Measured $\Delta_{471-CDES}$ (‰)	SE	N	Modeled $\Delta_{471-CDES}$ (‰)	Difference	Measured $\Delta_{48-CDES90}$ (‰)	SE	N	Modeled $\Delta_{48-CDES90}$ (‰)	Difference	Measured $\delta^{18}O_{VPDB}$ (‰)	SD	Modeled $\delta^{18}O_{VPDB}$ (‰)	Measured $\delta^{13}C_{VPDB}$ (‰)	SD	Measured $\delta^{13}C_{VPDB}$ (‰)
Mallinckrodt	0.477	0.003	9	0.477	0.000	0.207	0.023	5	0.207	0.000	-22.00	0.05	-22.01	-40.60	0.20	-40.56
Mix 1	0.583	0.006	17	0.580	0.003	0.246	0.012	7	0.247	0.001	-16.30	0.50	-16.88	-29.10	0.90	-29.92
Mix 2	0.584	0.005	18	0.584	0.000	0.249	0.014	10	0.249	0.000	-11.30	0.30	-11.76	-18.60	0.70	-19.28
Mix 3	0.491	0.007	21	0.494	-0.003	0.214	0.008	11	0.215	0.001	-6.40	0.30	-6.63	-8.20	0.50	-8.64
CM Tile	0.313	0.001	463	0.313	0.000	0.145	0.003	309	0.145	0.000	-1.50	0.00	-1.50	2.00	0.00	2.00

**Table 6.** Mixing model conditions for model data plotted in Figure 9, including experimental data using the internal carbonate standards Mallinckrodt and CM Tile as endmembers, and modeled endmembers with varying clumped and bulk isotope compositions. For the experimental data in Figure 9a, the largest  $\Gamma_{47}$  and  $\Gamma_{48}$  were observed when the mix contained 60% Mallinckrodt and 40% CM Tile, where  $\Gamma_i = \Delta_{\text{endmember}} - \Delta_{\text{mix}}$ .

Figure	Line color, symbol	Endmember	Initial $\Delta_{47\text{-CDES}}$ (‰)	Initial $\Delta_{48\text{-CDES90}}$ (‰)	Initial $\delta^{18}\text{O}_{\text{VPDB}}$ (‰)	Initial $\delta^{13}\text{C}_{\text{VPDB}}$ (‰)	$\Gamma_{47}$ (‰)	$\Gamma_{48}$ (‰)
9A	blue, circle	Mallinckrodt	0.477	0.202	-21.9	-40.5	0.117	0.045
		CM Tile	0.313	0.576	-1.5	2.0		
9B	red, square	E1	0.667	0.287	-10.0	-10.0	0.029	0.045
		E2	0.526	0.223	10.0	10.0		
	black, circle	E1	0.667	0.287	-10.0	-10.0	0.086	0.073
		E2	0.667	0.287	10.0	10.0		
	green, diamond	E1	0.667	0.287	1.0	1.0	0.000	0.000
		E2	0.526	0.223	1.0	1.0		
9C	black, triangle	E1	0.591	0.253	-30.0	-30.0	0.769	
		E2	0.591	0.253	30.0	30.0		
	blue, square	E1	0.591	0.253	-15.0	-15.0	0.193	
		E2	0.591	0.253	15.0	15.0		
	red, circle	E1	0.591	0.253	-5.0	-5.0	0.021	
		E2	0.591	0.253	5.0	5.0		
9D	black, triangle	E1	0.591	0.253	-30.0	-30.0		0.660
		E2	0.591	0.253	30.0	30.0		
	blue, square	E1	0.591	0.253	-15.0	-15.0		0.164
		E2	0.591	0.253	15.0	15.0		
	red, circle	E1	0.591	0.253	-5.0	-5.0		0.018
		E2	0.591	0.253	5.0	5.0		

**Table 7.** Comparison of measured and calculated  $\Delta_{47}$  and  $\Delta_{48}$  values. Experimental data from Swart et al. (2021) is from inorganic calcite precipitations. Fiebig et al. (2021) calculated values are based on a regression determined from experimental measurements of carbonates, including lake and cave calcite, inorganic precipitations, and samples equilibrated at high temperature, with samples having crystallization temperatures from 7.9 °C to 1100 °C. Lucarelli et al. (2021) and Bajnai et al. (2020) calculated values are based on regressions determined using a combination of theory from Hill et al. (2014) and Tripati et al. (2015) with experimentally determined acid digestion fractionation factors.

T (°C)	Measured values				Calculated values			Measured values			Calculated values			
	$\Delta_{47}^{14}\text{CDES}$ (this study) (‰)	SE	$\Delta_{47}^{14}\text{CDES}_{90}$ (Swart et al., 2021) (‰)	SE	$\Delta_{47}^{14}\text{CDES}$ (Lucarelli et al., 2021) (‰)	$\Delta_{47}^{14}\text{CDES}_{90}$ (Bajnai et al., 2020) (‰)	$\Delta_{47}^{14}\text{CDES}_{90}$ (Fiebig et al., 2021) (‰)	$\Delta_{48}^{13}\text{CDES}_{90}$ (this study) (‰)	SE	$\Delta_{48}^{13}\text{CDES}_{90}$ (Swart et al., 2021) (‰)	SE	$\Delta_{48}^{13}\text{CDES}_{90}$ (Lucarelli et al., 2021) (‰)	$\Delta_{48}^{13}\text{CDES}_{90}$ (Bajnai et al., 2020) (‰)	$\Delta_{48}^{13}\text{CDES}_{90}$ (Fiebig et al., 2021) (‰)
5	0.651	0.004	0.660	0.006	0.649	0.658	0.656	0.272	0.013	0.273	0.011	0.277	0.264	0.276
10	0.636	0.007	0.634	0.008	0.634	0.642	0.640	0.265	0.018	0.265	0.006	0.271	0.256	0.268
15	0.626	0.008	0.628	0.01	0.619	0.627	0.625	0.259	0.011	0.256	0.008	0.264	0.249	0.261
25	0.594	0.008	0.603	0.006	0.591	0.598	0.595	0.252	0.014	0.251	0.008	0.253	0.236	0.247
30			0.577	0.006	0.576	0.585	0.581			0.236	0.012	0.245	0.230	0.241
35			0.563	0.007	0.563	0.572	0.568			0.242	0.007	0.239	0.224	0.235
65			0.508	0.011	0.489	0.504	0.496			0.212	0.011	0.208	0.197	0.207

**Table 8.** Extra-sum-of-squares F test results which determines if regressions have significant differences between them and if all datasets can be represented by one combined regression. Experimental regressions for samples with known precipitation temperature were used from Swart et al. (2021), Fiebig et al. (2021), and this study. An additional comparison was performed using an experimental  $\Delta_{17}$  and  $\Delta_{18}$  regression with samples of unknown precipitation temperature, including standards, from Lucarelli et al. (2021). The regressions from Bajnai et al. (2020) and Lucarelli et al. (2021) based on theory from Hill et al. (2014) and Trinalli et al. (2015) with experimental AFFs were then compared to the experimental regressions.

	Comparison of Fits	Source of regression	Null hypothesis	Alternative hypothesis	P value	Conclusion (alpha = 0.05)	Preferred model	F (DFn, DFd)
<b>Experimental regressions</b>	$\Delta_{17}$ and $\Delta_{18}$	Swart et al., 2021; Fiebig et al., 2021; this study	One curve for all data sets	Different curve for each data set	0.99	Do not reject null hypothesis	One curve for all data sets	0.03 (6, 43)
	$\Delta_{17}$ and $\Delta_{18}$	Swart et al., 2021; Fiebig et al., 2021; Lucarelli et al., 2021; this study	One curve for all data sets	Different curve for each data set	>0.99	Do not reject null hypothesis	One curve for all data sets	0.05 (8, 57)
	$\Delta_{17}$ and $10^3 T^{-2}$	Swart et al., 2021; Fiebig et al., 2021; this study	One curve for all data sets	Different curve for each data set	0.99	Do not reject null hypothesis	One curve for all data sets	0.13 (6, 43)
	$\Delta_{18}$ $10^3 T^{-2}$	Swart et al., 2021; Fiebig et al., 2021; this study	One curve for all data sets	Different curve for each data set	0.99	Do not reject null hypothesis	One curve for all data sets	0.03 (6, 43)
<b>Experimental regressions with regressions based on theory with experimental AFFs</b>	$\Delta_{17}$ and $\Delta_{18}$	Bajnai et al., 2020; Swart et al., 2021; Fiebig et al., 2021; Lucarelli et al., 2021; this study	One curve for all data sets	Different curve for each data set	0.99	Do not reject null hypothesis	One curve for all data sets	0.18 (10, 62)
	$\Delta_{17}$ and $10^3 T^{-2}$	Bajnai et al., 2020; Swart et al., 2021; Fiebig et al., 2021; Lucarelli et al., 2021; this study	One curve for all data sets	Different curve for each data set	0.99	Do not reject null hypothesis	One curve for all data sets	0.26 (10, 53)
	$\Delta_{18}$ $10^3 T^{-2}$	Bajnai et al., 2020; Swart et al., 2021; Fiebig et al., 2021; Lucarelli et al., 2021; this study	One curve for all data sets	Different curve for each data set	0.99	Do not reject null hypothesis	One curve for all data sets	0.12 (10, 53)